Wide field imaging with the recirculator

A huge great enormous thing, like -- like nothing. A huge big -- well, like a -- I don't know -- like an enormous big nothing ...

Piglet describes Heffalump
in *Winnie the Pooh*
by *A.* **A. Milne**

Chapter 4

WIDE FIELD IMAGING WITH THE RECIRCULATOR

'The visibilities measured with different delay settings are processed off-line to get the final images over a wide field in declination. The processing involves detection of interference, calibration of the visibilities of different delay zones, transforming[1] the visibilities to brightness distribution, regridding the images to a common epoch, combining the images of different days of observations and then deconvolving to get the final image. In this chapter, we discuss the data processing stages of interference detection, calibration, transformation of visibilities to brightness distribution and combining the images of different sets (days) of observation.

4.1 Interference

We discussed some aspects of the protection of radio frequencies in astronomy in Chapter 1. There we noted that with progress in technology, the. demand

---

[1] The recirculator which measures visibilities with different delays could be used to get the images in smaller bands. This way of imaging is also known as spectral line synthesis wherein the brightness distribution from the sky is measured as a function of direction and frequency. This would require us to have measurements with the same delay settings on all the baselines. However, the visibilities from short baseline in the first round of observations were measured without the recirculator. We therefore have not been able to use spectral line synthesis for imaging with the recirculator.

for the usage of the electromagnetic spectrum is increasing. The development is so fast that a clean band space for passive users, such as of radio astronomy, is becoming ever so scarce. Even though several spectral bands have been protected for Radio Astronomy (Table 1.2), the pressure for making more spectral space commercially usable is extreme. Although these commercial usages are important, often the extreme vulnerability of passive users is not fully appreciated, resulting in unwanted emissions (RFI) in the radio astronomy bands.

The growing use of satellite systems and the practice of placing communication repeaters on the peaks of mountain ranges are making it difficult to find any place on the earth which is free from interference and is safe for doing radio astronomy. Radio astronomy at low frequencies is becoming particularly difficult because of the increased use of communication systems at these frequencies.

The Mauritius Radio Telescope, with its low operating frequency of around 150 MHz and antennas with a broad primary beam, is very susceptible to terrestrial interference. Interference causes spurious features in an image. If these effects are greater in strength than the noise fluctuations, they lead to misinterpretation. Hence, it is important to remove this interference.

Some of the known sources of interference are communication systems, ignition systems and other arcing sources, satellites and the active Sun. Many of these produce short-interval, 'spiky' interference which has frequency components at a much higher frequency than that of the response of the antenna to celestial sources. Interference from man-made sources is highly polarized. Interference from communication systems is also generally narrow-band. However, interference with a broader spectrum is produced by arcing sources. There is also interference created "in-house" – these are generally harmonics from oscillators used in the instruments in the observatory and from oscillations of malfunctioning amplifiers used in the system.

The Mauritius radio telescope was designed to work at a center frequency of 150 MHz. However, because of heavy interference in the 1 MHz band around it from terrestrial and from some unidentified satellite(s), we shifted the observing frequency to 151.5 MHz. The 1 MHz band around this frequency is relatively free from interference.

At the MRT, since we do not measure the polarization of the signal, we cannot use this property of interference in differentiating the interference from the sky signal. Furthermore since we use XF correlators, we cannot reject parts of the observing band in which the interference occurs and use the rest of the band.

We found the power supplies of the PCs to be the main source of RFI emanating from the observatory building. These and the other parts of the receiver system were shielded by putting them in grounded Faraday'cages. The analog and digital parts were grounded separately. Since the telescope site is rocky, the natural grounding is not good. Three pits, each 3 m deep, with copper grounding plates buried in a mixture of coal and salt were used to improve the grounding. Two of these were used to separately ground the digital and analog parts of the receiver system. The third pit was used as ground for the air-conditioners and the computer systems outside the receiver room. The observatory building was not constructed with shielding. We reduced the effect of interference from the observatory by covering, with grounded stainless steel mesh, those walls which are facing the array.

To reduce the effect of common-mode interference picked up by the first IF cables and by the second IF signal lines, phase switching of the LO was implemented (Section 2.1.4). We were also faced with the noise generated by the LO generator at 30 MHz, the first IF frequency. This leaked to the IF port at the first mixer and produced high correlations in some of the baselines. To reduce this, we put a high-pass filter in the path of the LO. To further reduce the spurious emission from the LO generator, we shifted the frequency of our first LO from the initially used 181.6 MHz to 121.6 MHz, where the level of noise generated was much lower. Since we did not have filters around this frequency, to suppress the noise at 30 MHz from the LO synthesizer and from other LO amplifiers, band-reject filters at 30 MHz were implemented using power splitters with bandpass filters centered at 30 MHz (Figure 2.10). These were placed at the output of the LO synthesizer and at the outputs of the amplifiers in the LO distribution system.

Pick-up in the 1 MHz band around 50 MHz also comes into the observing band on heterodyning the first IF with an LO of 40 MHz. To reduce their effects, we introduced filters[2] centered at 30 MHz just before the heterodyning with the 40 MHz LO.

After sorting out most of the problems related to "in-house" interference, we still had interference in our data from external sources. Generally the interference seen was 'spiky' in nature. We now discuss the techniques developed for detecting this kind of interference at the MRT.

4.1.1 Interference Detection

Interference which is 'spiky' in nature has Fourier components beyond the maximum due to the sky signal. In interferometer arrays, the visibility data is generally sampled in time at rates much faster than the rates required for a

---

[2] These filters were earlier placed in the field after the first mixers and were moved into the laboratory for observations from block-3 onwards.

given baseline. This oversampling can be made use of in identifying interference which is 'spiky' in nature. For example, at the MRT the baseline with the longest east-west component ($\sim 512\lambda$) has a maximum fringe rate of about 0.04 Hz (see footnote **3)**. We would therefore need to sample this data at 0.08 Hz to satisfy the Nyquist sampling criterion. We have sampled the data at about every one second which allows us to identify frequencies up to 0.5 Hz. Therefore interference can be identified by its contribution to frequencies in the range 0.04 Hz to 0.5 Hz.

The maximum frequency[3] to which the sky contributes at the output of a complex correlator is given by $\omega_e x$, where $\omega_e = dH/dt = \frac{2\pi}{(24*60*60)} = 7.27\times10^{-5}$ radians per sidereal second and x is the east-west component of the baseline in wavelengths. Since x depends on the baseline used, the ability to distinguish interference from the sky signal decreases with increasing east-west component of the baseline. To overcome this baseline dependence, instead of detecting interference in the *cos* and the *sin* channels separately, interference is detected in the magnitude domain, i.e., in $\sqrt{\cos^2+\sin^2}$. The magnitude of visibility has a rate of change which is independent of the baseline used. This rate depends on the primary beam of the interferometer which is the product of the voltage patterns of the group of antennas forming the interferometer. The expected maximum frequency at the MRT in the magnitude of the visibility is $\sim$0.003 Hz.

If we had no a *priori* information about how the interference affects different baselines, we would need to detect interference on the *sum* of *magnitudes*

---

[3] The fringe frequency $f_{osc} = \frac{1}{2\pi}\frac{d\phi}{dt}$ = kg x $\frac{dH}{dt}$ where $\phi = 2\pi(x\xi + y\eta + z\zeta)$. Since the fringing is predominantly due to the east-west component of the baseline, the fringe frequency may be approximated as $f_{osc} = \frac{1}{2\pi}\frac{d}{dt}(2\pi x.\xi) = x\cos H\cos\delta$ x $\frac{dH}{dt}$. In terms of u where $u = x\cos\mathrm{H}$, the fringe frequency is $\omega_e u\cos\delta$ where $\omega_e = dH/dt = \frac{2\pi}{(24*60*60)} = 7.27\times10^{-5}$. The fringe rate is fastest for a source at $\delta = 0$ and is $\omega_e u$. For small H, i.e., near the meridian $\cos\mathrm{H} \approx 1$ and therefore $\omega_e u = \omega_e x$.

obtained by summing all possible combinations of baselines for best detection. For example, if the interference had affected only two interferometers, then this interference would best be detected if the detection was carried out on the summation of magnitudes of these two baselines only, instead of adding the contribution of all the baselines. This, however, is not practical in terms of the time it would take. We find that generally, interference affects all baselines simultaneously. Therefore, to improve the detectability of interference we add the magnitudes of all the visibilities used. We refer to this combined data as the sum of magnitudes.

At the MRT we measure 512 baselines per second. Of these, 480 (15×32) baselines are used for imaging. If the magnitudes of all the visibilities of these 480 baselines are added, we will be able to detect interference of the level of $4\sigma_m\sqrt{480}$ with a 4σ detection, where a, is the RMS noise on the $\sqrt{cos^2 + \sin^2}$ of any baseline and a is the RMS noise on the sum of magnitudes. For statistical considerations, a detection level greater than four times the RMS of the noise is used. Assuming interference affects all baselines with equal strength, we are able to detect interference down to $4\frac{\sigma_m}{\sqrt{480}}$, i.e., $\frac{\sigma_m}{5.5}$ per baseline. On the other hand if only n baselines are affected, then an interference of strength less than $\frac{4\sigma_m\sqrt{480}}{n}$ per baseline would go undetected[4].

The noise in the an image made with N days will be $\sqrt{2}\frac{\sigma_m}{5.5}\sqrt{N}/\sqrt{\tau_{integ}}$, where τ_{integ} is the post-integration applied. For simplicity, assuming that there is interference at a given sidereal time on only one of the N days, the ratio of undetected interference to the noise in the image will be $\frac{\frac{4\sigma_m}{\sqrt{480}}}{\sqrt{2}\frac{\sigma_m}{\sqrt{480}}\sqrt{N}/\sqrt{\tau_{integ}}} \sim$

---

[4] We are assuming that interference affects all the baselines with equal strength. For the general case of interference affecting different baselines with different strengths the detection criterion of $\frac{\sum_{i=1}^{n} w_i}{\sqrt{480}\sigma_m} = 4$ would need to be satisfied, where w_i is strength of the interference in the i^{th} baseline.

$2.83\sqrt{\frac{\tau_{integ}}{N}}$. The final image is made by combining 60 days of data. For this image with $\tau_{integ} = 16$ seconds the undetected interference will be of the order of the noise.

Ideally, the process of combining visibilities of different baselines may also be extended to the data of different days to further detect interference which occurs at the same RA on some other day. We would need to detect interference on all possible combinations of different days being combined for best detection. This is not a very practical solution because for 60 sets of data the number of combinations is huge. So, for the time being, we will allow undetected interference of the order of the noise in the final images. This, in terms of flux density, will be of the order of 100 mJy.

By detecting interference in the sum of magnitudes (incoherent detection), the sensitivity to detection will be $\sqrt{2}$ times worse than if the detection was carried out on phased visibilities (coherent detection). In using sum of magnitudes, there is the advantage of detecting interference with the same sensitivity, independent of phasing. Hence any interference which is greater than $4\sigma_m/\sqrt{480}$ per baseline and changes at a rate faster than the primary beam of the interferometer can be distinguished.

4.1.2 Implementation scheme

In the implementation of the detection of interference, the sum of magnitudes is low-pass filtered. This is done by applying a rectangular window function on the Fourier transform of the sum of magnitudes data. This retains only those frequencies corresponding to the sky contribution. The low pass filter allows a maximum frequency of $\omega_e x$, where x is the maximum east-west spatial frequency . For an EW x NS interferometer, x = 36X. The output of this filter, which contains frequencies up to $\omega_e x$, is Inverse Fourier Transformed (IFT) to a time series. This is then subtracted from the visibility data resulting in the 'difference' data from which the sky contribution has been removed. This 'difference' data is basically a high pass data with frequencies greater than $\omega_e x$, i.e., greater than what the sky response can give. This therefore may be considered to consist only of contributions from the receiver noise and from the interference. The interference is detected in this 'difference' data. The detected points are stored in a file and are used to reject these points in subsequent processing. The flow diagram shown in Figure 4.1 summarizes the technique used.

We now look at the different ways we tried detecting the interference to minimize the time required without losing the reliability of the detections.

We started with the brute-force method in which the maximum deviation is located in the 'difference' data. If this deviation is greater than $k\sigma$, it is noted as interference. σ is the expected RMS deviation due to the receiver noise in the 'difference' data and k determines the threshold level of detection. This noted point is then removed from the time series in both the cos channel and the *sin* channel. The magnitude of the remaining data is passed through the high pass filter again. This process is repeated iteratively, till no points beyond $k\sigma$ are detected in the 'difference' data.

This method although simple and effective is prohibitively slow as it requires a filtering operation (involving an FFT and an IFT) for every interference point.

To reduce the time required we tried out an algorithm in which the interference is treated as a set of delta functions. In the 'difference' data a delta function appears convolved with the high pass function. In this algorithm, the

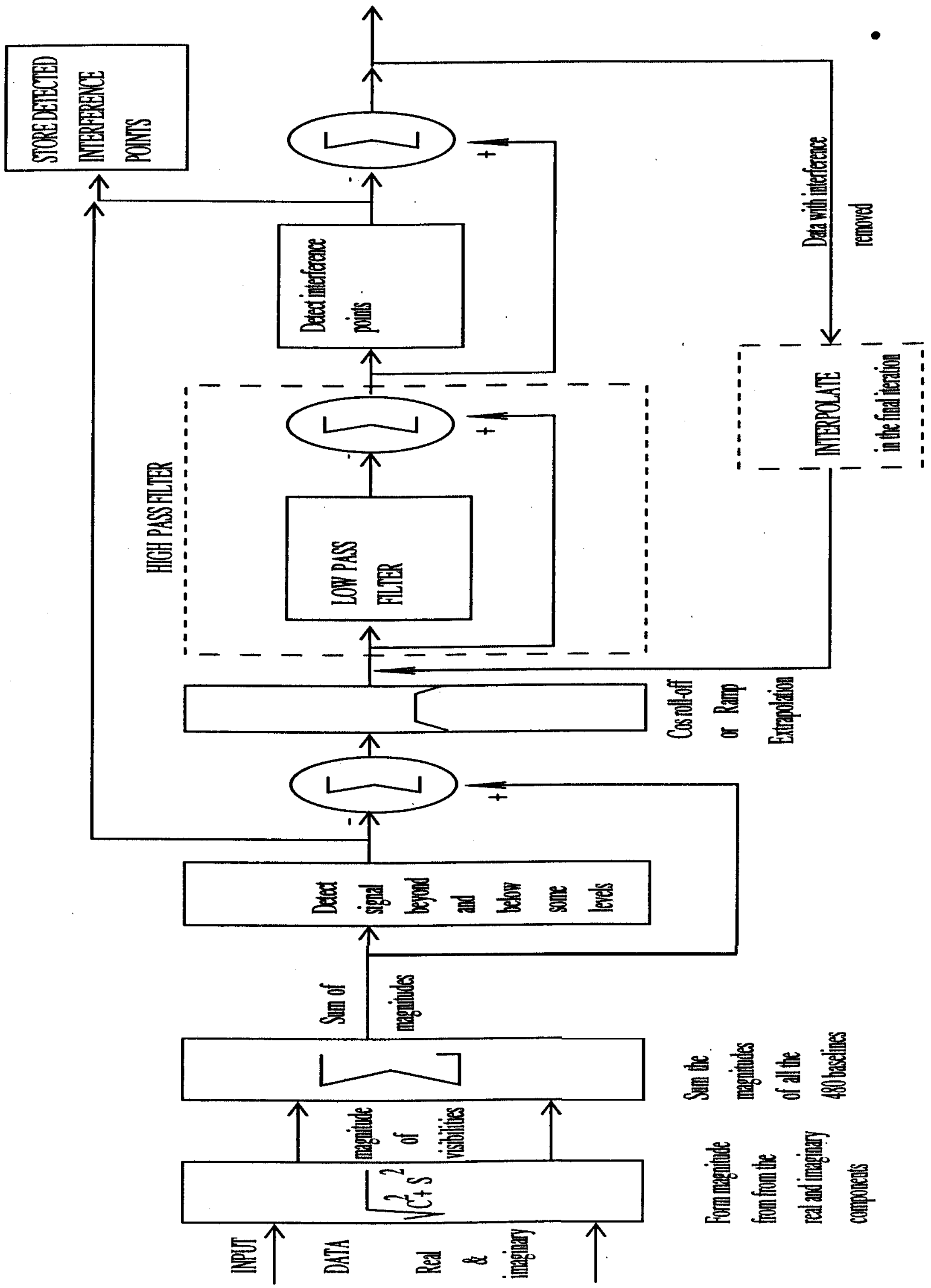

Figure 4.1: Block diagram illustrating the method adopted for interference detection.

maximum greater than $k\sigma$ is detected as earlier. However, instead of removing the marked out point in the time series and doing the whole process all over again, the high-pass response of a delta function of strength equal to the detected interference is subtracted from the 'difference' data. The next highest point is then removed and so on. This is essentially performing a 'CLEAN' on the 'difference' data. All detected points are then removed from the visibility data in one go.

Some erroneous detections occur if there are strong, closely spaced interference which results in a very distorted 'difference' data. To overcome such a problem the following alternative algorithms were tried out:

(a) Whenever an interference point is found, a scaled high pass response due to the interference (which is the response of the high pass filter to a delta function) is removed . This is similar to introduction of a 'loop gain' in a standard CLEAN.

(b) The interference is detected in the 'difference' data above a certain threshold level which is set depending on the maximum interference level. In each iteration interference points of strength greater than 80% of the peak interference detected are removed. Although, this method generally requires more iterations than method (a), we found that this method gives better results and is therefore used in the final implementation of interference detection.

A few practical aspects in interference detection are listed below.

1. Because of offsets[5] on some correlator outputs, $\sqrt{cos^2 + \sin^2}$ has higher frequency components than the cut-off criterion used[6]. In the *sum* of

---

[5] These correlator offsets are generally within 2σ of noise.

[6] $\sqrt{(A+\cos(\omega t))^2 + (B+\sin(\omega t))^2} = \sqrt{A^2 + B^2 + 1 + 2A\cos(\omega t) + 2B\sin(\omega t)} = \sqrt{A^2 + B^2 + 1 + K cos(\omega t - \phi)}$. A and B are the offsets in the cos and the *sin* channels respectively. $\phi = \tan^{-1} \frac{B}{A}$ and $K = 2\sqrt{A^2 + B^2}$.

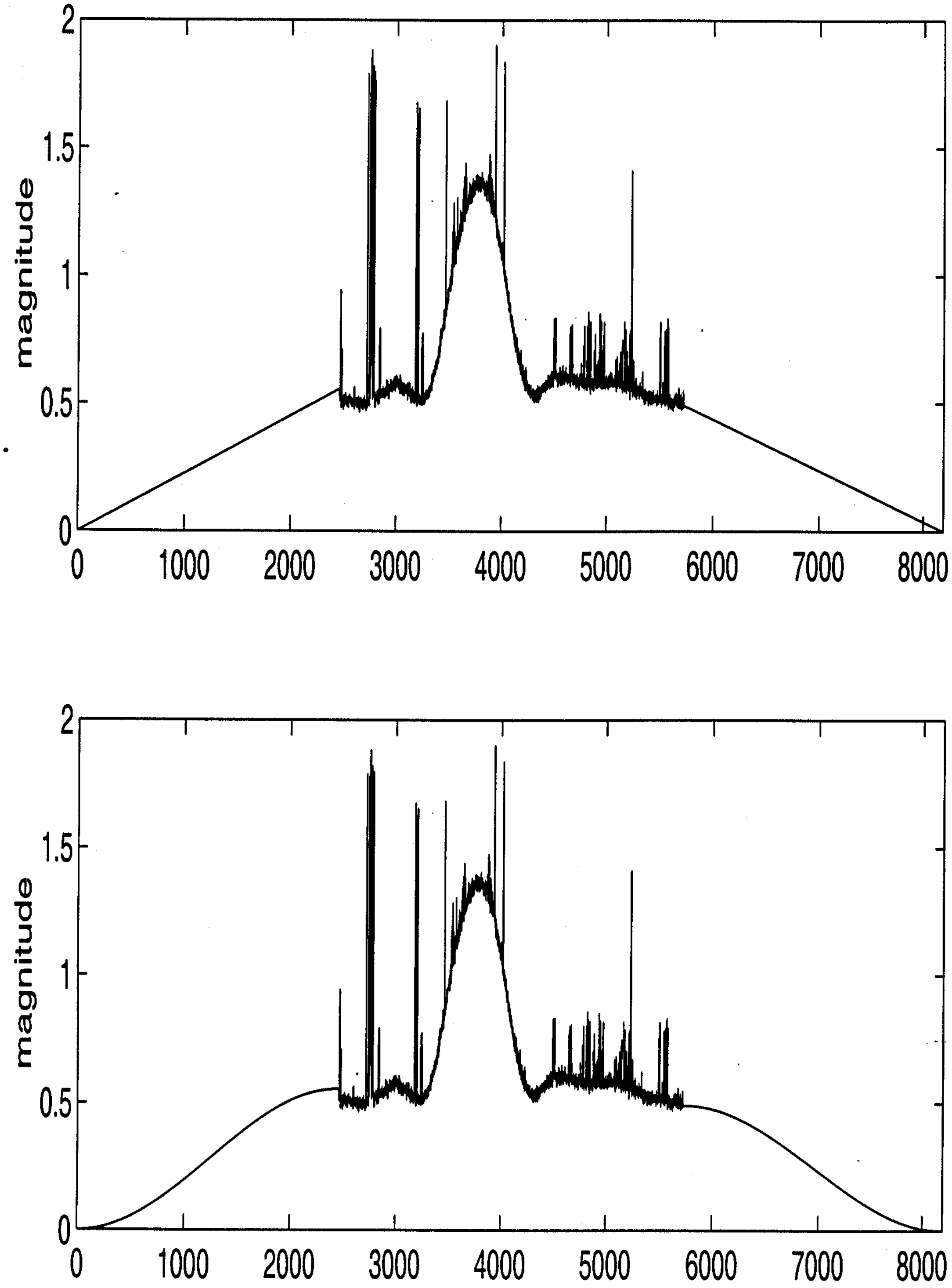

Figure 4.2: Extrapolation: The data at the beginning and at the end of the file are extrapolated with (a) a ramp function (ramp extrapolation) (b) cosine roll-off function.

the magnitudes, the contribution of these frequency components due to different baselines is only $\frac{1}{480}$ and therefore these are not detected as interference. But one would need to take this into account when applying the technique on lesser number of baselines where the contribution of the fringing component produced by the offsets could be significant.

2. Using a DFT causes ripples whenever there is an offset between the beginning and the end of the patch being Fourier transformed [7]. Depending on the strength of the ripple, this may be detected as interference. To overcome this, the data at the beginning and at the end of the file are extrapolated with a smooth function before performing any DFT. We find that using a cosine roll-off or a ramp function for extrapolation is generally sufficient. An example of the ramp extrapolation and cosine roll-off extrapolation is shown in Figure 4.2. The cosine roll-off is better because it does not have a discontinuity at the edges. A larger extrapolation results in a smoother transform. The more standard practice would be to use windowing which would require data before and after the patch over which we are trying to detect interference. Using the 'smoothing' extrapolation we are able to process any size of data without requiring the data before and after the patch of interest.

3. Response due to a strong source partially appearing at the beginning or at the end of a patch being processed will have a rate of change much higher than that expected from the sky and therefore would get removed as interference. This is prevented by increasing the length of the extrapolating function at the edge whenever a source of significant strength ($\geq 30\sigma$ in the sum of magnitudes) is encountered at the edge of

---

[7] In a DFT algorithm the patch being transformed is treated as being periodic

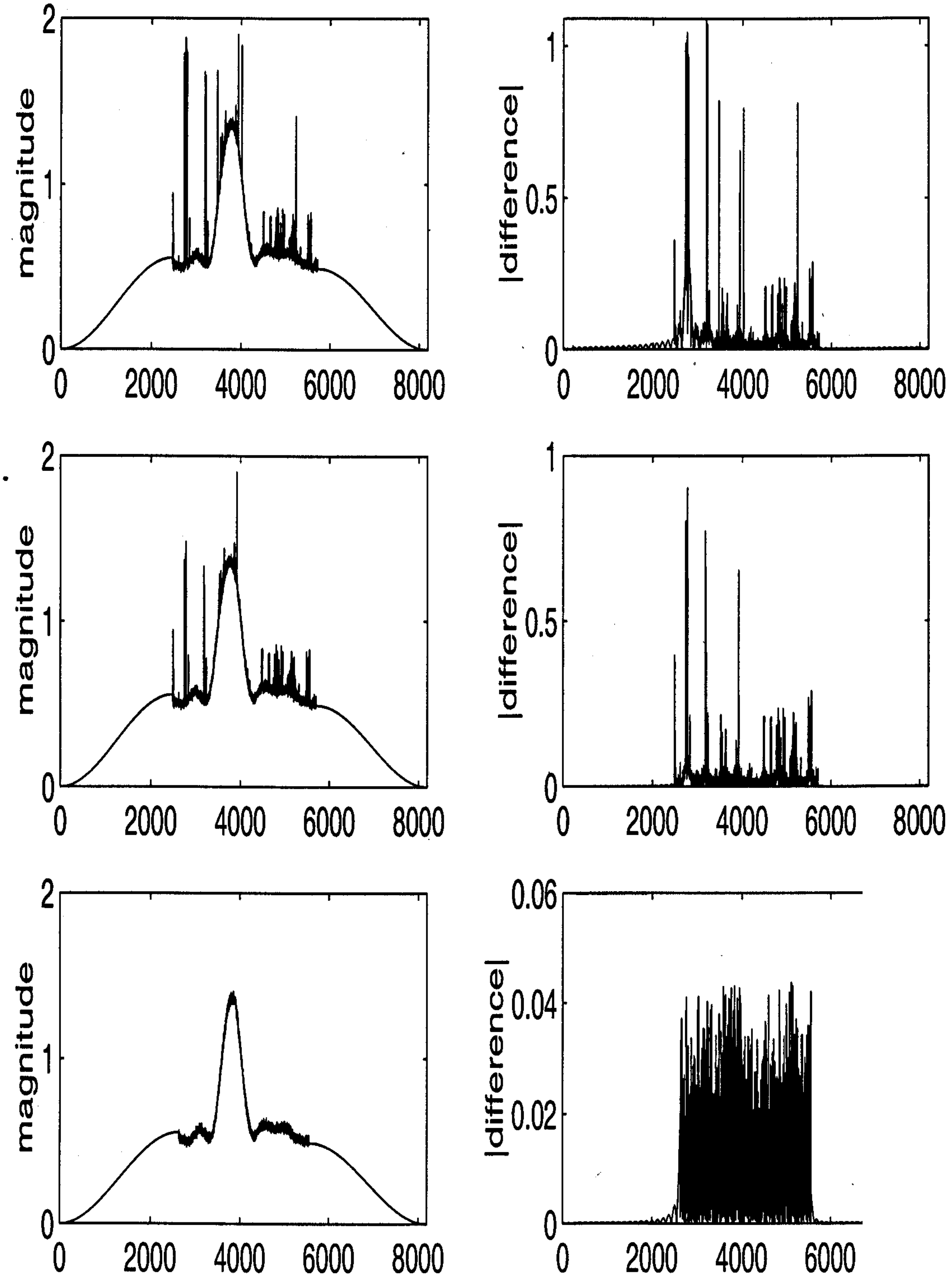

Figure 4.3: The different stages in interference detection. The left column plots show the extrapolated *sum of magnitudes* and the right column plots show the corresponding 'difference' data. The results of the $1^{st}, 5^{th}$ and the 15^{th}, which is the last iteration, are shown.

a patch being processed.

4. An upper-cutoff and a lower-cutoff level are introduced based on *a priori* information of the highest and the lowest levels of the signals from the sky for a given patch being processed. Any data point which is larger than, or less than, the limiting value is expunged from the data before any filtering is done. This reduces the time to process interference detection as the number of iterations are greatly reduced. The cut-off levels for any sidereal time take into account the changes in the Sun's RA.
5. Slowly varying interference is not detected by our procedure. Hence we also examine the difference between *sum of magnitudes* of two days (same trolley allocation) after removal of interference and interpolation.
6. As a final measure, the *sum of magnitude* plots after interference removal and interpolation are visually inspected and any suspicious looking data is manually identified.

At the MRT, programs have been developed to implement the described algorithm. The process of interference detection has been automated (except steps 5 and 6) and is carried out at the end of each sidereal hour. An example of the different stages in interference detection is shown in Figure **4.3** with the column on the left showing the *sum of magnitudes* and the column on the right shows the corresponding 'difference' data. Figure 4.4 shows all the interference points which have been detected. The *sum of magnitude* after removal of the interference points and interpolation is shown in Figure 4.5.

The raw data is not modified by the interference detection programs. The detected points are stored in a file and this information on interference is used

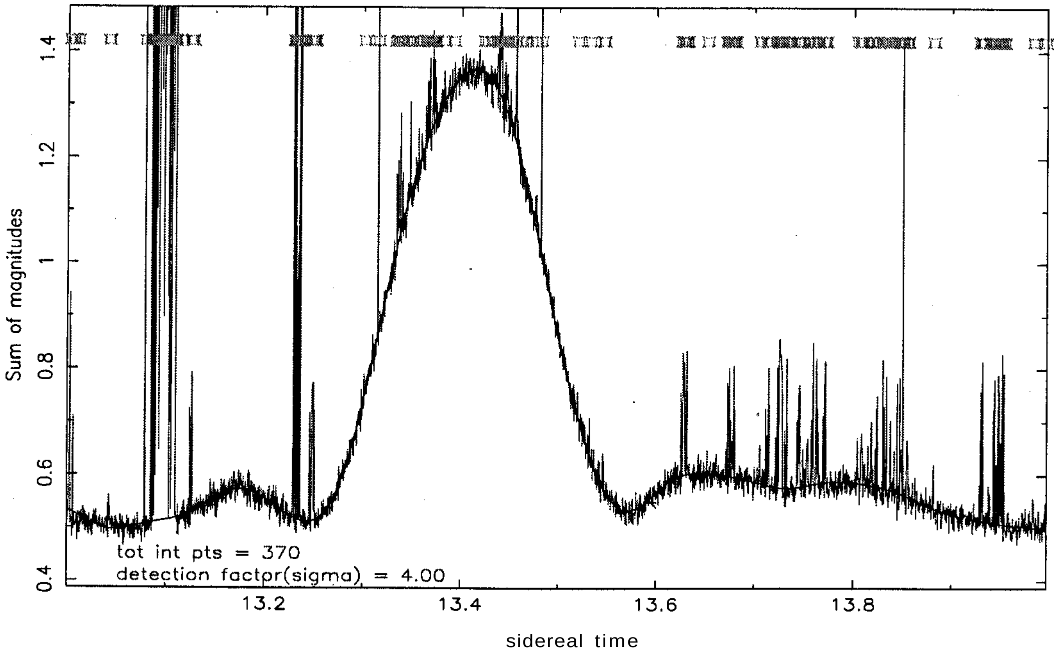

Figure *4.4:* Interference detection on the *sum* ***of*** *magnitudes:* Detected interference points are marked out. Overlaid on the data is the fit to the data after removal and interpolation of the interference points from the *sum* ***of*** *magnitudes.*

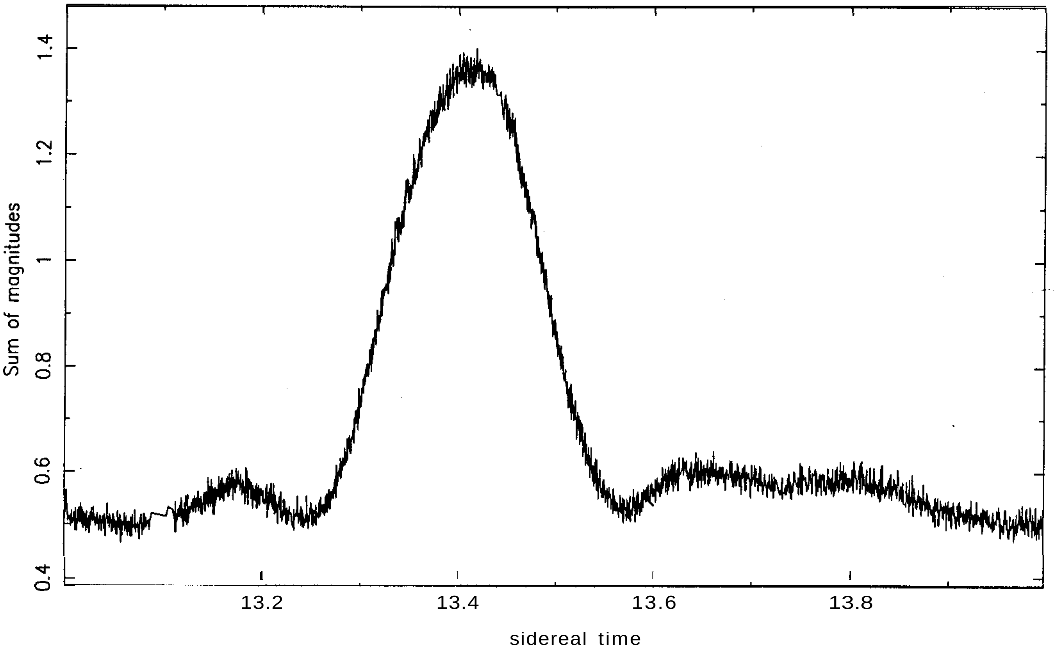

Figure *4.5: Sum* ***of*** *magnitudes* after removal of interference and interpolation.

in the subsequent calibration and imaging programs which we discuss in the later sections of this chapter.

4.1.3 Statistics of detected interference

We have data from observations over a year and have carried out interference detection on most of this data. We now look at the statistics of the detected interference.

We note that we do not have any frequency information of the interference. However, we find that generally, the strength of the interference is correlated in the different delay zones and therefore the interference is narrow-band (less than 10 kHz) in nature.

A typical histogram of the number of interference points against their strengths is shown in Figure 4.6.

From the histogram we note :

- The number of low strength interference is larger and most of the interference has strengths less than 100σ. Interference of strength greater than about 1300 are very few.
- The number of interference points peaks for interference strength in the range 50 and 10σ.

Figure 4.7 is a histogram of interference points against strength of interference up to about 5000.

- The number of interference points do not fall monotonically and occasionally there is a large number of interference points at around 700 and 100σ.

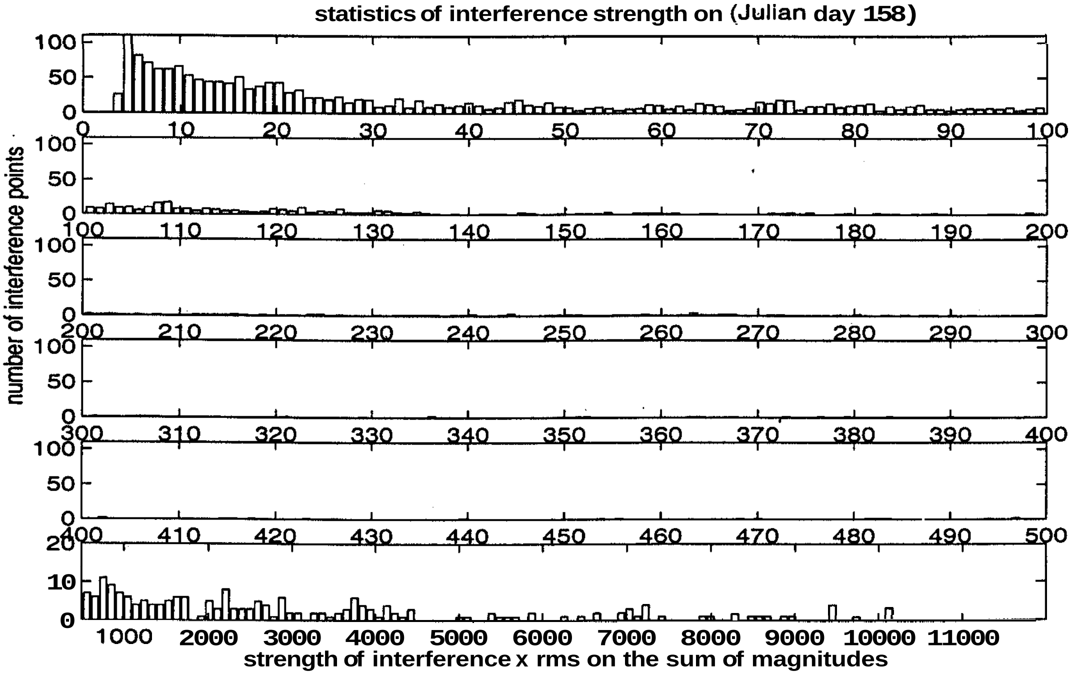

Figure 4.6: Histogram of number of interference points versus the strength of interference. All plots have 100 bins. (a) up to 100σ (b) from 100σ to 2000 (c) from 2000 to 3000 (d) from 3000 to 4000 (e) from 4000 to 5000 (f) from 5000 to max interference level

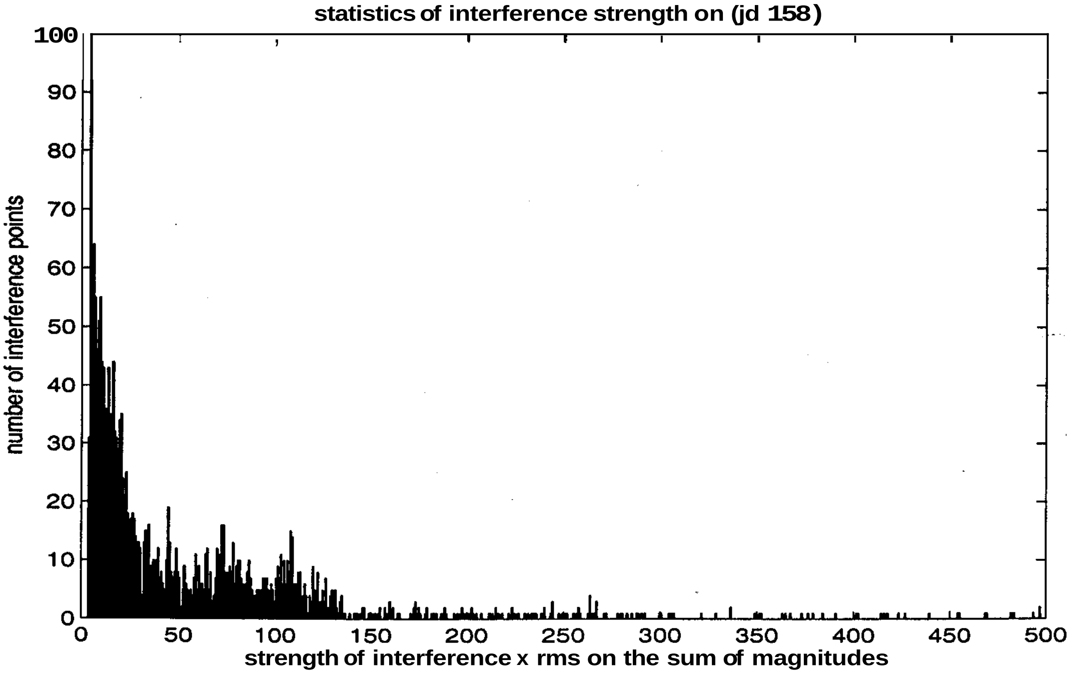

Figure 4.7: Histogram of number of interference points versus the strength of interference of up to 500σ.

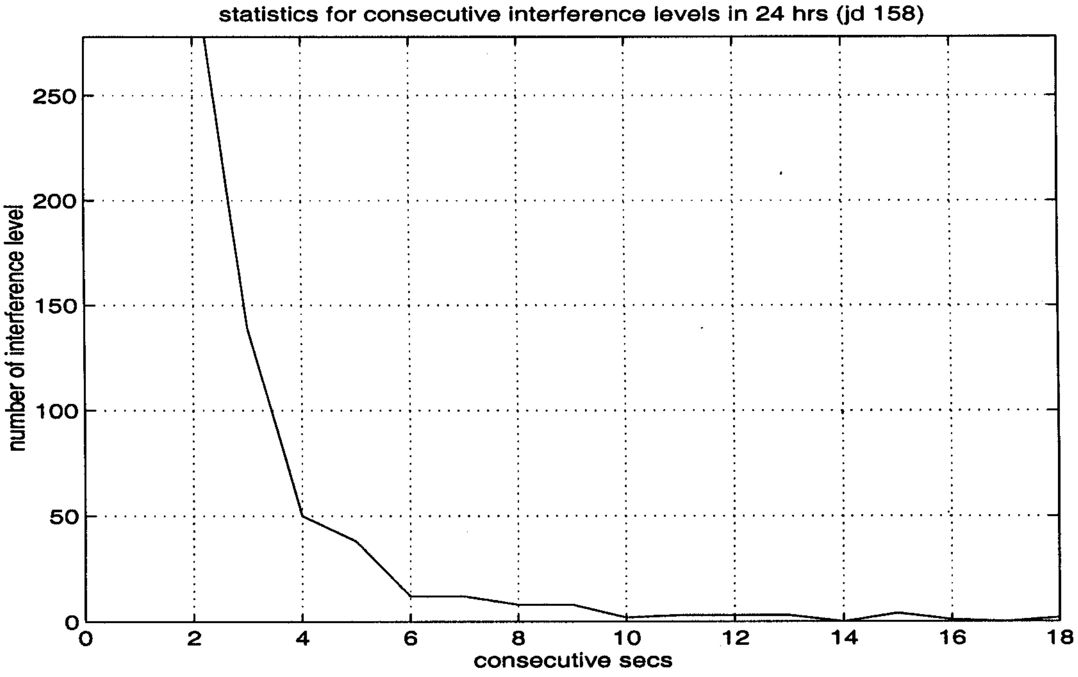

Figure 4.8: Statistics of the duration of interference.

Figure 4.8 shows the number of interference against number of consecutive seconds an interference lasts.

- We see that the largest number of interference occur for shorter durations. There are generally less than 20 instances in the full 24 hours when the interference lasted 6 consecutive seconds. This statistic indicates that very often the interference excision can be carried out while post integrating by giving a zero weighting to the interference points.

A typical plot of number of interference against local time in a given day is shown in Figure 4.9.

- The interference is largely during the day and is mainly between MST[8] 8:00hrs and 15:00hrs. These are the industrial working hours in Mau-

---

*Mauritius Standard Time.

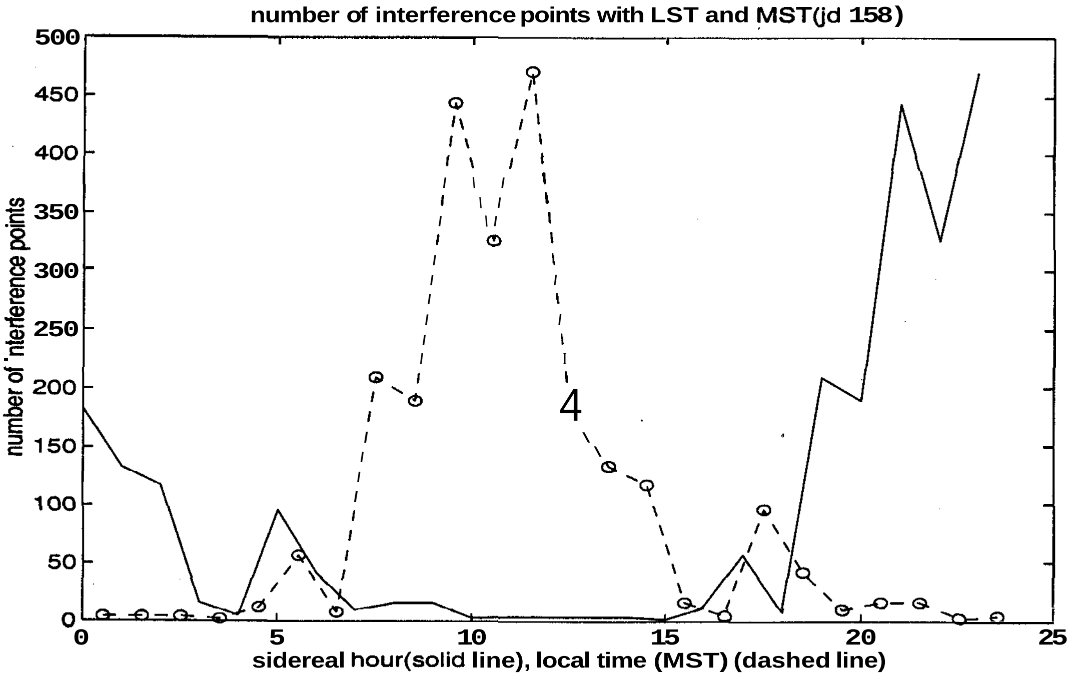

Figure 4.9: Number of interference points with LST and MST.

ritius. This therefore indicates that interference is linked to the local industry.

Figure 4.10 shows the number of interference points on different days during the observing period.

- We don't see any particular trend in the number of interference over the year. A better indicator of any trend would require analysis of statistics of a larger number of days.

- Although the sources of interference are not identified, we have found that the interference is drastically reduced on Sundays and on other public holidays. As is seen from the Figure 4.10, there is very little interference on Julian days JD 2450250 and JD 2450320, which are both Sundays.

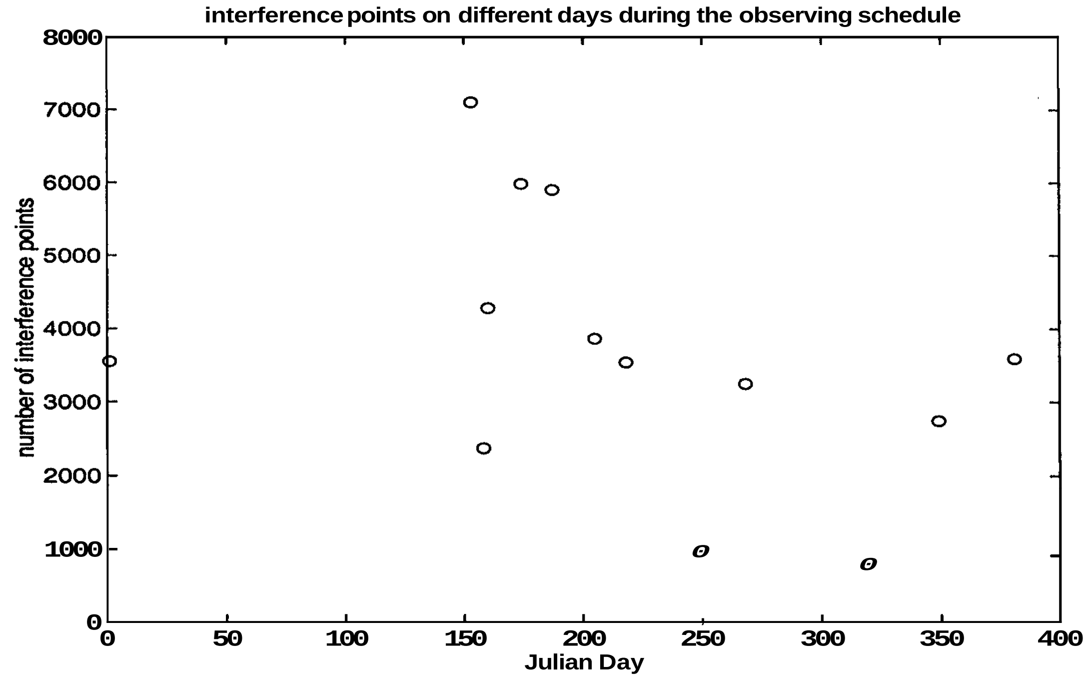

Figure **4.10:** Number of interference points on different days during the observing schedule. The Julian days are shown truncated. The 0 on the x-axis corresponds to Julian day **2450150.**

4.2 Antenna Calibration

The next stage of data processing after interference detection involves calibration. In this section we discuss some aspects of calibrating the observed data.

4.2.1 Calibrating the visibilities

During actual observation of some brightness distribution $B(\xi, \eta)$, we measure $V_{obs}(x, y, z)$, which is the true visibility $V(x, y, z)$ multiplied with the complex gain $G(x, y, z)$ of the interferometer, plus the stochastic complex zero-mean noise $\beta(x, y, z)$ and the baseline based complex offset $\epsilon(x, y, z)$ (also referred to as DC offset).

$$V_{obs}(x,y,z) = V(x,y,z) \times G(x,y,z) + \beta(x,y,z) + \epsilon(x,y,z) \qquad (4.1)$$

The true visibilities are obtained from the measured visibilities by the process of calibration wherein the effect of the instrument is removed to a large extent. The efficacy of calibration is determined by the signal-to-noise ratio in the measurement. Methods such as self-calibration, redundant baseline calibration or observation of a region of known brightness distribution are generally used to calibrate the complex gains of the interferometers used. The present calibration technique used at the MRT is based on the observation of a known strong point source.

Any measured visibility may be expressed as a sum of contributions due to several point sources in the field of view each of strength A_i and a location (ξ_i, η_i). Therefore the observed visibility can be written as

$$V_{obs}(x,y,z) = \sum_i G(x,y,z)\ A_i A(\xi_i,\eta_i) e^{j2\pi(x\xi_i+y\eta_i+z\zeta_i)} + \beta(x,y,z) + \epsilon(x,y,z) \tag{4.2}$$

where $A(\xi_i, \eta_i)$ is the power pattern of the interferometer.

We now consider calibration using one of the point sources, generally a strong one, in the primary beam of the helix. Knowing the source strength A, and its co-ordinates (ξ_o, η_o) at any instant, we can estimate the complex gain $G(x, y, x)$ of the interferometer. The contribution to the visibility due to this source is $A(\xi_o, \eta_o) A_o e^{j2\pi(x\xi_o+y\eta_o+z\zeta_o)}$.

By multiplying the observed visibility over time with the expected complex conjugate of the expected visibility and averaging the product over time, i.e., by computing $< V_{obs} V_{exp}^* >$, we, in principle, can estimate the complex gain of the interferometer[9]. We refer to this method of calibration as fringe calibration. Multiplication with a term $e^{-j2\pi(x\xi_o+y\eta_o+z\zeta_o)}$ removes the ξ, η, ζ dependence from the term of interest leaving us with:

---

[9] This is similar to extracting the gain of a Fourier component in a Fourier series.

$$
\begin{aligned}
< V_{obs}V^*_{exp} >=< V_{obs}(x,y,z)A_oA(\xi_o,\eta_o)e^{-j2\pi(x\xi_o+y\eta_o+z\zeta_o)} > \\
= \frac{1}{N}\sum A_oA(\xi_o,\eta_o)G(x,y,z) \\
\times A_iA(\xi_i,\eta_i)e^{j(2\pi(x(\xi_i-\xi_o)+y(\eta_i-\eta_o)+z(\zeta_i-\zeta_o)))} \\
+\beta(x,y,z)A_oA(\xi_o,\eta_o)e^{-j2\pi(x\xi_o+y\eta_o+z\zeta_o)} + \epsilon(x,y,z)A_oA(\xi_o,\eta_o)e^{-j2\pi(x\xi_o+y\eta_o+z\zeta_o)}
\end{aligned}
\tag{4.3}
$$

At the MRT the east-west group beam limits the hour-angle (H) range over which the source is seen to H=±1° about the meridian. Over this range, the temporal fringe rate due to the y and the z components of the baselines is negligible and the fringing is mainly due to the changing east-west component of the baselines. If Equation **4.3** above is averaged over hour-angle such that $2\pi x(\xi - \xi_o)$ for any source undergoes complete cycles, then for all such sources the average tends to zero. The terms $\epsilon(x,y,z)A_oA(\xi_o,\eta_o)e^{-j2\pi(x\xi_o+y\eta_o+z\zeta_o)}$ and $\beta(x,y,z)A_oA(\xi_o,\eta_o)e^{-j2\pi(x\xi_o+y\eta_o+z\zeta_o)}$ also tend to zero on the average. It can therefore be shown that Equation **4.3** reduces to

$$
< V_{obs}V^*_{exp} >= \frac{1}{N}\sum G(x,y,z)A_o^2A^2(\xi_o,\eta_o) \tag{4.4}
$$

Where $G(x,y,z) = |G(x,y,z)|e^{j\phi_{ins}(x,y,z)}$

which is the weighted average of the complex gain[10]. Each point in the summation is weighted by a^2 where $a = A_oA(\xi_o,\eta_o)$ is the S/N on the calibrator. $A(\xi_o,\eta_o)$ is equal to the product of the voltage patterns of the antenna

---

[10] For an interferometer of an east-west group and a north-south group, the weighting is given by:

$$
A_oA(\xi,\eta) = A_o\frac{1}{32}\frac{\sin\left(\frac{32\psi}{2}\right)}{\sin\left(\frac{\psi}{2}\right)}P(\xi,\eta) \times \frac{1}{4}\frac{\sin\left(\frac{4\psi}{2}\right)}{\sin\left(\frac{\psi}{2}\right)}P(\xi,\eta) \tag{4.5}
$$

where $P(\xi,$ I)) is the primary beam response of an individual helix.

groups forming the interferometer and the point source strength. This weighting with the square of the signal-to-noise ratio while averaging gives the best estimate of the complex gains.

Baselines with short east-west component

For baselines with small east-west components, the integral will not be zero over H= ±1° range of integration since $2\pi x(\xi - \xi_o)$ does not go through complete cycles in this hour angle range. Also, short baselines are sensitive to the large scale structure of the Galactic background. Therefore, fringe calibration does not work well for baselines with a small east-west component, except for very strong calibrators. To estimate the complex gain (phase and amplitude) of these baselines we use closure information obtained with the last east-west group E16 (Section **2.2**). Since E16 is multiplied with all the east-west groups and all the south groups, the gain of a short baseline like S1E1 is derived from measurements of S1E16 and E1E16.

$$\frac{G_{S1,E16}G_{E16,E1}}{G_{S1,E1}G_{E16,E16}} = \frac{(G_{S1}G^*_{E16})(G_{E16}G^*_{E1})}{(G_{S1}G^*_{E1})(G_{E16}G^*_{E16})} = 1 \qquad (4.7)$$

therefore

$$G_{S1,E1} = \frac{G_{S1,E16}G_{E16,E1}}{G_{E16,E16}} = \frac{|G_{S1}||G_{E16,E1}|e^{j(\phi_{S1}-\phi_{E16})}|G_{E16}||G_{E1}|e^{j(\phi_{E16}-\phi_{E1})}}{|G^2_{E16}|} \qquad (4.8)$$

The sensitivity per baseline at the MRT is 30 Jy for a 1 MHz bandwidth and an integration time of one second. In 10 minutes of time which is the time taken taken by sources at −40° to transit a 2 degree beam, we get a sensitivity per baseline[11] of about 2 Jy. However, because of contributions

---

and

$$\psi = \frac{2\pi}{\lambda}(d\xi) = \frac{2\pi}{\lambda} d \sin H \cos\delta \qquad (4.6)$$

[11] The non-uniform weighting due to the primary beam has to be taken into account in calculating the sensitivity.

Source name (1950)	RA (1950)	Dec (1950)	Expected flux density at 150 MHz (Jy)	NS primary beam factor b
MRC 0915-119	09 15 43	-11 52 00	290	0.51
MRC 1932-464	19 32 18.4	-46 27 00	87	0.97
MRC 2211-173	22 11 21	-17 15 00	80	0.66

Table 4.1: The calibrators used at the MRT.

from sources other than the main calibrator in the primary beam, we need stronger calibrators to get reliable calibration. We find that only three sources give good and consistent calibration for the MRT. These sources are given in Table 4.1

Apart from the general limitation imposed by the S/N of the calibrators and the broad primary beam (leading to substantial contributions from sources other than the main calibrator), there are other factors which affect the calibration of the array. Some of these are the stability of the system, timing and positional errors, and accurate knowledge of bapdshapes [36]. These are discussed in the following sections.

4.2.2 System Stability

Due to lack of suitable calibrators in our primary beam, we need to look at the stability of our system to be able to apply calibration obtained at one time to the data at other times. For this we check the variation in instrumental gain (phase and amplitude) from one day to another on the same source and from one source to another at different times of the day.

We have found that the day-to-day RMS variation per baseline in phase is about 10° and the RMS amplitude variation is about 0.1 dB. Typical histograms of the difference in the instrumental phase and amplitude of the baselines estimated using MRC 1932-464 on two consecutive days (JD 2449997 and

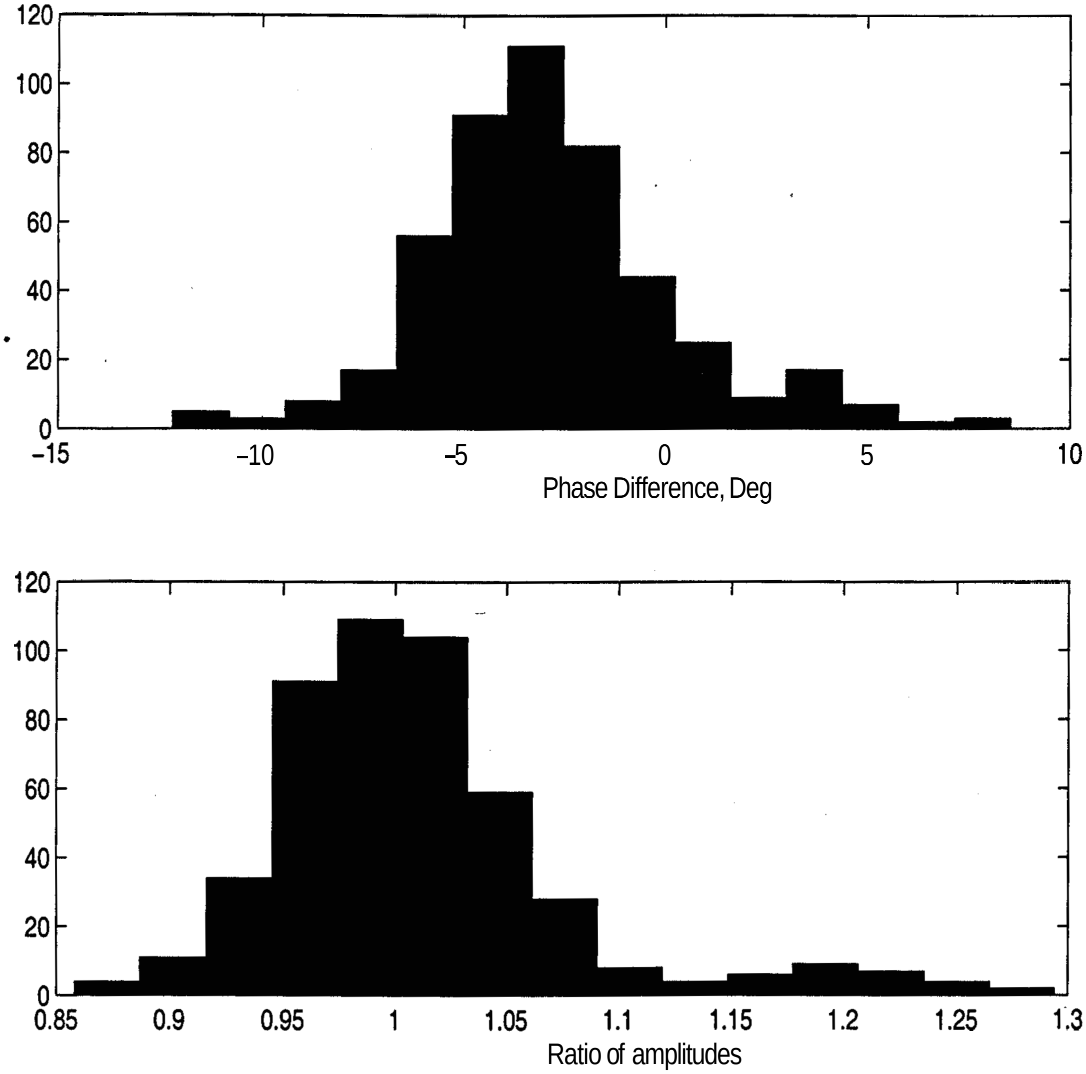

Figure 4.11: Histogram of difference in phase (top plot) and the ratio of amplitudes (bottom plot) of the instrumental gains of the baselines estimated using MRC 1932-464 on two consecutive days.

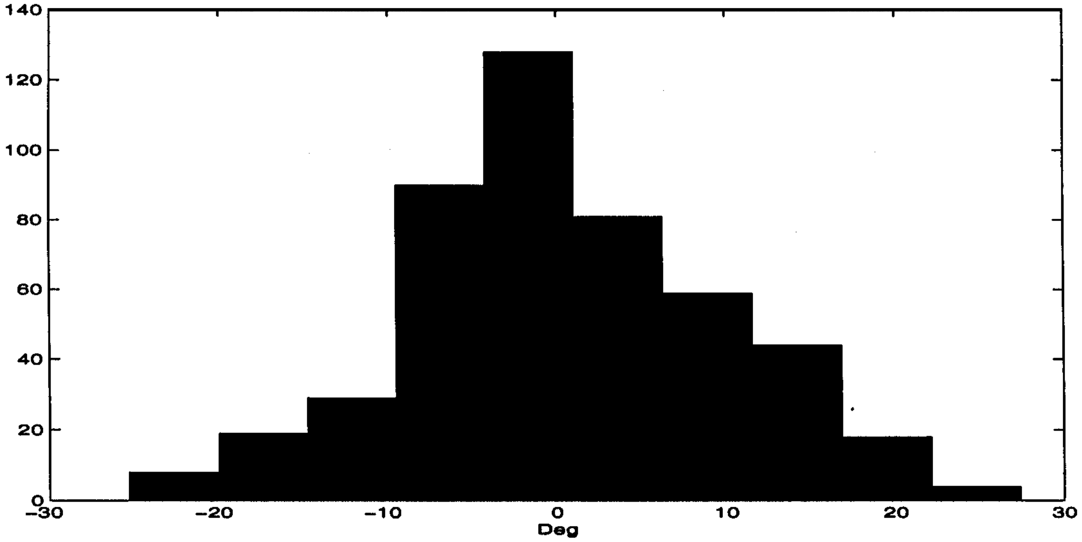

Figure 4.12: Histogram of the difference in instrumental phases estimated using two different calibrators (MRC 1932-464 and MRC 0915-119). The RMS variation of the difference in phases is typically about 10°.

JD 2449998) are shown in Figure 4.11.

The RMS variation of phase of the baselines from one calibrator to another (e.g. MRC 1932-464 and MRC 0915-119) is also about 10°. Figure 4.12 shows the typical difference in instrumental phase between one source and another. These variation include effects due to ionospheric variation over the day as well.

4.2.3 Timing Errors

Timing errors and accurate knowledge of the positions of the antennas are crucial in estimating the baseline gains. For estimating these errors, we compare the instrumental phases obtained by using calibrators at different declinations. Errors in the position of the telescope and errors in position of the source give similar errors in calibration.

A timing error results in an error in the assumed hour angle for the calibrators. Let H and H_1 be the true and the assumed angles respectively, then the difference between the instrumental phases obtained from the calibrators at declination δ_1 and δ_2 is given by

$$\begin{aligned}\Delta\phi &= 2\pi[x.(\sin \mathrm{H} - \sin H_1)(\cos\delta_2 - \cos\delta_1)\\ &+y.\sin\phi(\cos \mathrm{H} - \cos H_1)(\cos\delta_2 - \cos\delta_1)\\ &+z.\cos\phi(\cos H - \cos H_1)(\cos\delta_2 - \cos\delta_1)] \qquad (4.9)\end{aligned}$$

For small hour angles of ±1° the first term dominates and the other two terms do not contribute significantly. Therefore, the phase difference $\Delta\phi$ can be written as

$$\Delta\phi = 2\pi x\Delta H(\cos\delta_2 - \cos\delta_1) \qquad (4.10)$$

From the above equation we see that when the instrumental phases of two calibrators with different declinations are compared, an error in time stamping the data results in a gradient in the derived instrumental phase across the east-west arm.

The timing errors are estimated for each 24 hour observation. The errors were mostly zero in all the observations except those in block-3 and block-4. In block-3 (172 m-261 m) and block-4 (262 m-351 m) the sidereal clock used for time stamping the data was ahead[12] of the true time by about 54 seconds. Figure 4.13 shows the difference between instrumental phases estimated using calibrators MRC 0915-119 and MRC 1932-464. The different lines are for each north-south trolley. The gradient along the east-west in this plot indicates an error of 54.1 seconds in the clock. This error has been taken care of at various stages of data processing.

---

[12] This was due to an error in the program used to convert the local time to sidereal time. So although the sidereal clock was set almost everyday, we were setting it wrong during first round of observation in these two blocks. This was then corrected and in all subsequent observations there are no timing errors.

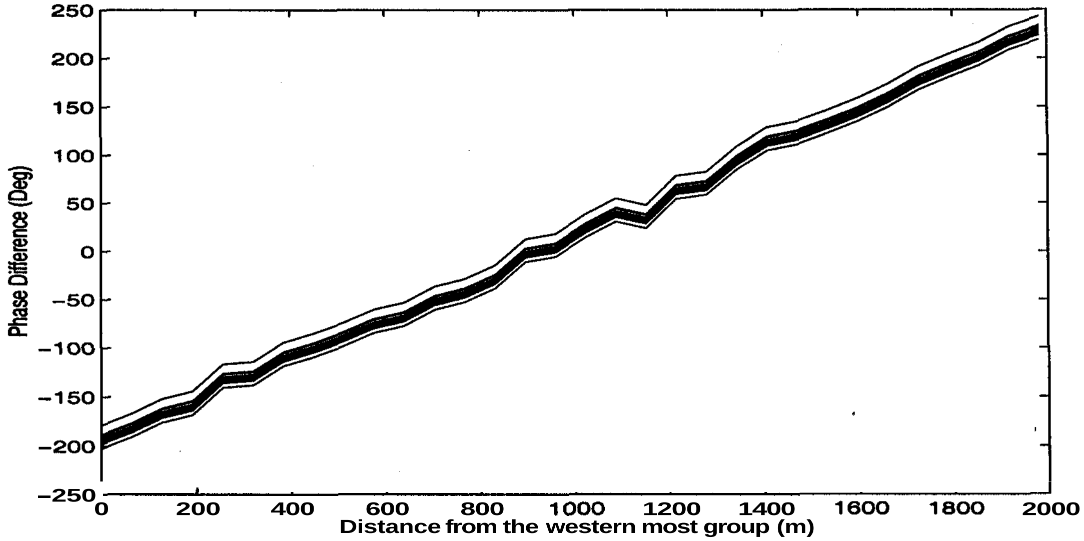

Figure 4.13: Plot showing the phase gradient along the east-west arm due to an error of 54.1 sidereal seconds in the astronomical clock.

4.2.4 Positional errors

The errors in relative positions of different trolleys and groups results in the difference in the instrumental phases obtained from calibrators at different zenith angles.

If the errors in the x, y, z co-ordinates of the baselines are Ax, Ay and Δz, then the error in calibration phase may be written as

$$\Delta\phi = 2\pi(\Delta x.\xi + \Delta y.\eta + \Delta z.\zeta) \tag{4.11}$$

During calibration, we take an average over the hour angle range of ±1°.

$$\begin{aligned}\Delta\phi = \sum_{H_i} 2\pi[\Delta x(\cos\delta\sin H_i) + \mathrm{Ay}(\cos 6\cos H_i\sin\phi - \sin\delta\cos\phi) \\ +\Delta z(\cos\delta\cos H_i\cos 4 + \sin 6\sin\phi)]\end{aligned} \tag{4.12}$$

Since H_i is taken only ±1°, the above equation can be written as

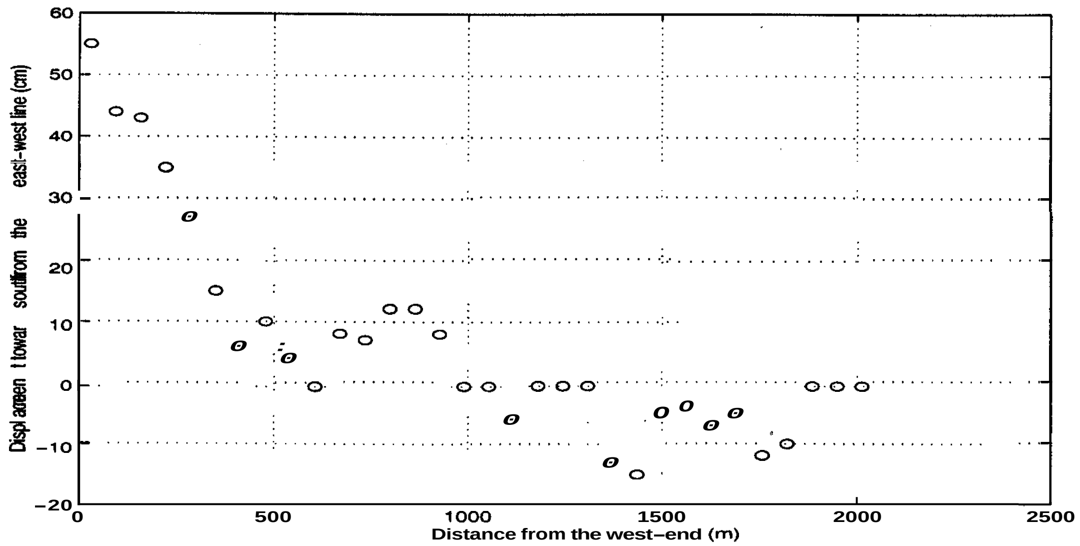

Figure 4.14: Displacement of the 32 east-west groups from the true east-west line.

$$\Delta\phi = \sum_{H} 2\pi(\Delta x \cos\delta \sin H_i + \Delta y \sin(\delta - \phi) + \Delta z \cos(\delta - \phi)) \tag{4.13}$$

If the summation is done symmetrically about the transit, then the $\sum_{H_i} 2\pi\Delta x \cos\delta \sin H_i$ term tends to zero leaving us with a phase errors dependent on Δy and Δz.

$$\Delta\phi = 2\pi(\Delta y \sin(\delta - \phi) + \Delta z \cos(\delta - \phi)) \tag{4.14}$$

Using three sources at different zenith angles along the meridian, we can solve for *Ay* and *Az*. Once the errors in *y* and z have been taken care of, we can do the summation unsymmetrically about transit in Equation 4.13 with *Ay* $= 0$ and *Az* $= 0$, to get the errors in *x*. We found that some groups in the east-west arm were away from the true east-west line with a maximum displacement of 55 cm towards the south. Figure 4.14 shows the displacement of the groups from the true east-west line. The initial markings on the north-south track

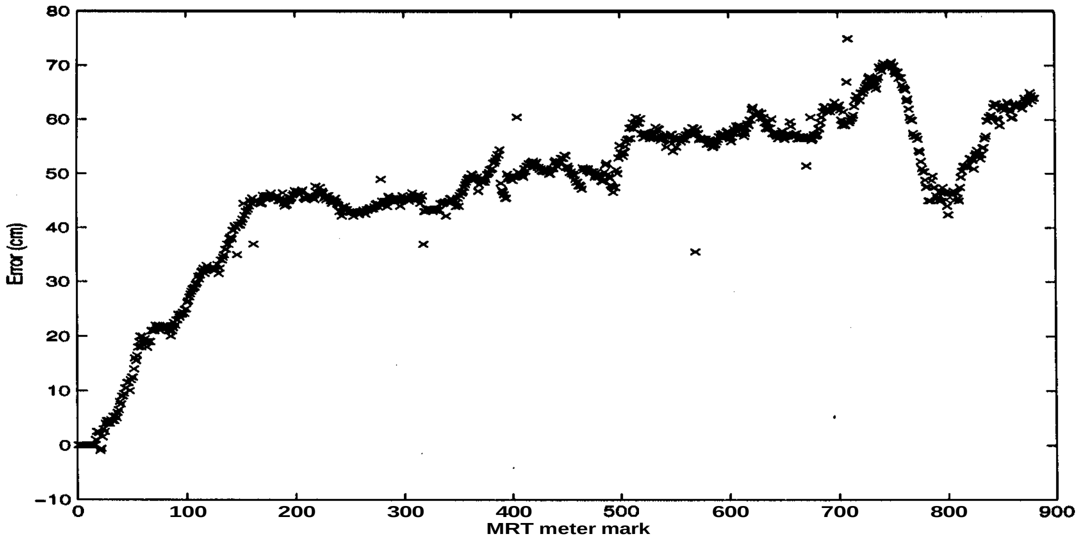

Figure 4.15: Error in marked positions along the north-south rail track.

were also found to be in error. The measurements along the rail-track have been carried out using a tension-tape to an accuracy of a centimeter. These measurements agree with those found using the calibrator sources for baselines up to about 200 m. The position measurements beyond 200 m have not been confirmed using the calibrator sources and will be undertaken in the future. A plot of errors along the track with the markings is shown in Figure 4.15. We found the marked position to be less than the true value in almost all markings with the maximum error of about 70 cm. A plot of height measurements using water levels is shown in Figure 4.16. The accuracy of these measurements are also believed to be within a centimeter. The height measurements indicate that there are two distinct slopes in the south track. Till about 655 m, the south track has a downward slope of $\frac{1}{2}^\circ$ and from there onwards, it has an upward slope of 1°. These new estimates of the positions are included in the allocation files which are used to determine the positions of the groups while processing the data.

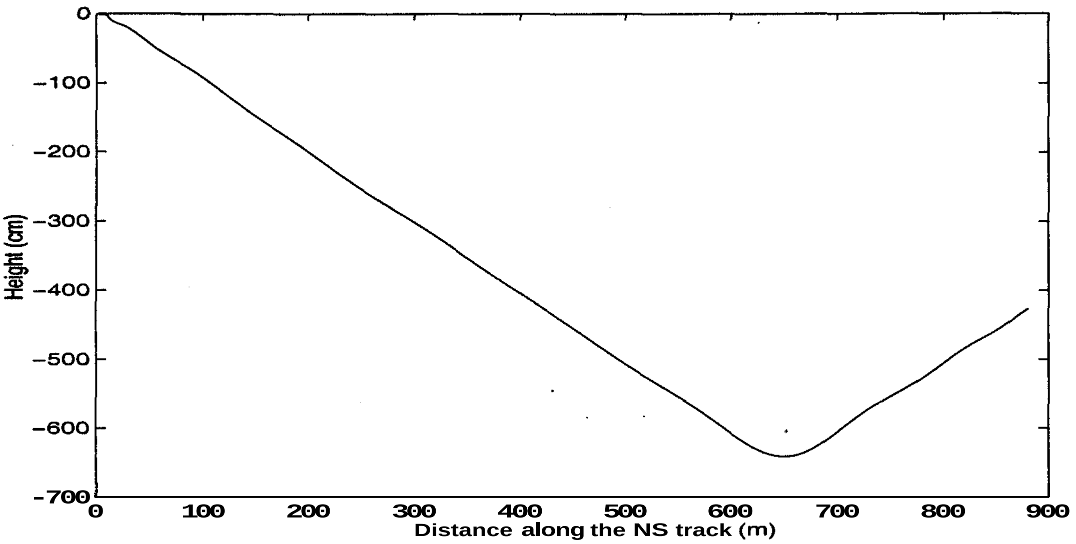

Figure 4.16: The heights along the north-south rail track.

4.2.5 Delay zone calibration

The recirculator system was designed to observe with different delay settings. Each delay setting maximizes the correlation in a given range of declination, which is called a delay zone. For imaging different delay zones, one has to calibrate visibilities measured with different delay settings. An ideal calibration scheme would be one in which we use separate calibrators in each declination zone. However we do not have sufficient number of strong calibrators in the southern sky to calibrate the visibilities in the different delay zones. Hence we were forced to use the complex antenna gains estimated for one zone, in which we have a strong calibrator, to calibrate the other zones. To appreciate how the method adopted works, let us consider the response of an interferometer for different delay settings.

The response of an interferometer as a function of the delay settings depends on whether it is a double sideband (DSB) or a single sideband system (SSB). A DSB system is one in which both the upper and the lower sideband responses are accepted. In a simple conventional DSB system, the RF signal is brought to the baseband by heterodyning with an LO placed at the frequency of interest, and the observing band is chosen by a narrow-band video filter much narrower than the RF band. Such a DSB system responds like a single frequency interferometer. This frequency is the LO frequency itself, provided the RF band can be considered flat over twice the bandwidth of the video filter. This is satisfied in most of the receiver systems. Thus in a DSB, it is easy to fix the interferometer baseline without knowing the details of the video bandshape. Any delay setting in the video part of the receiver causes linear phase gradients in the two sidebands in the opposite directions, ensuring the instrumental phase calibration to be independent of the delay setting. 'This is not true in an SSB system since it is difficult to achieve symmetrical narrow band IF filters identical in all the channels. In the next section, we discuss the response of the SSB system used at the MRT.

4.2.5.1 Single sideband system of the MRT .

The single sideband correlator setup of the MRT is shown in Figure **4.17** [37]. All the relevant equations for this SSB interferometer are also given in this figure. The correlator response $C(\tau)$ of an interferometer obtained by integrating the single frequency response over the cross power spectrum may be written as:

$$C(\tau) = \gamma(|\tau_D - \tau|)|G|e^{j(2\pi\overline{\nu_{if}}(\tau_D-\tau)-2\pi(lo_1+lo2)\tau+\phi_{inst})} \tag{4.15}$$

where τ is the geometrical delay, τ_D is the compensating digital delay and $\gamma(|\tau_D - \tau|)$ is the bandwidth decorrelation term (fringe washing term). This is the Fourier transform of the cross power spectrum. lo_1 and lo_2 are the first and the second local oscillator frequencies respectively. G is the complex gain of the interferometer expressed in terms of the magnitude $|G|$ and the phase

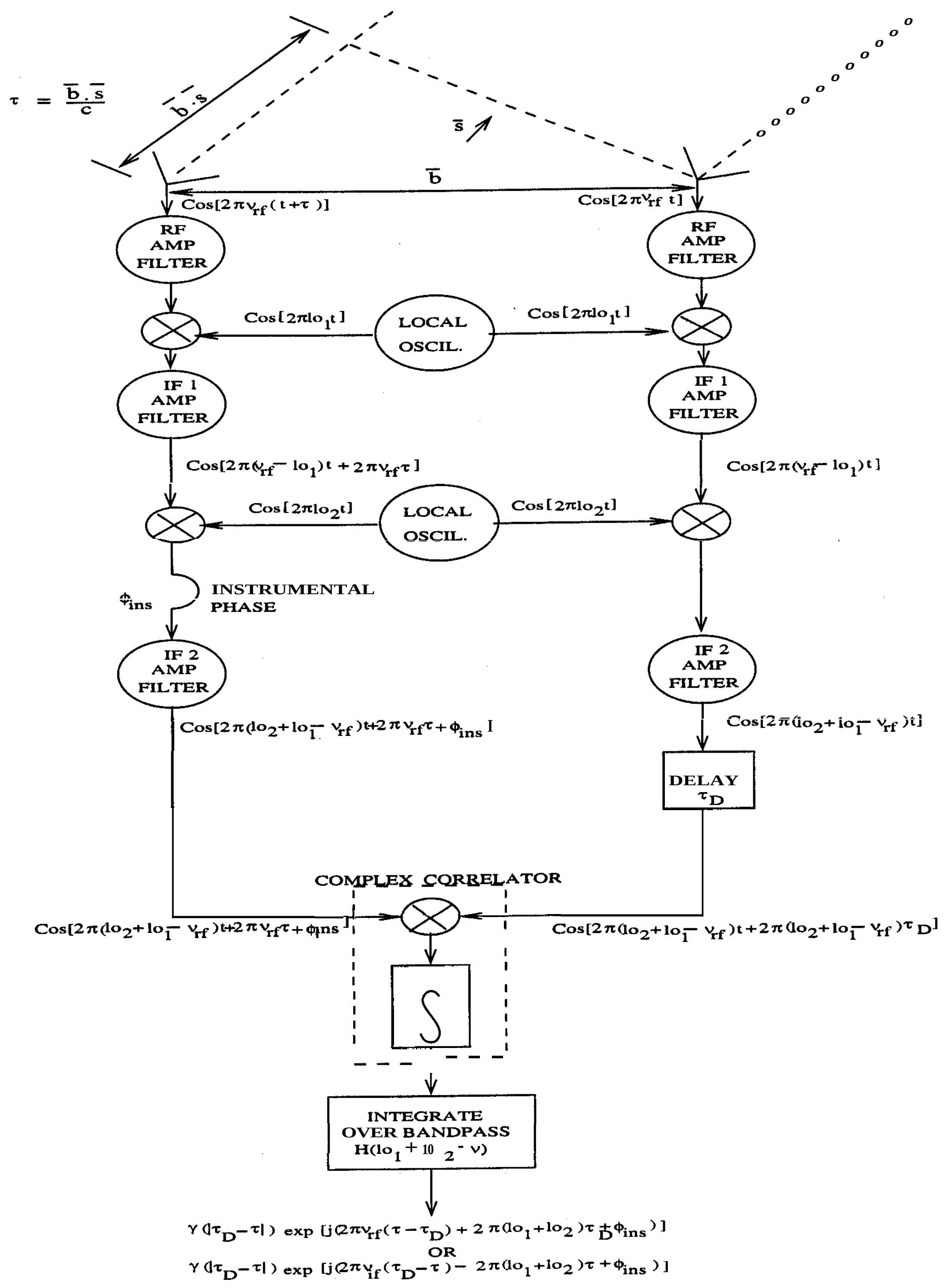

Figure 4.17: Schematic of the single sideband correlator system of the MRT.

ϕ_{inst}, i.e., $\mathbf{G} = |G|e^{j\phi_{inst}}$. The equivalent IF frequency of operation, $\overline{\nu_{if}}$, is defined as the centroid of the cross power spectrum.

$$\overline{\nu_{if}} = \frac{\int_0^\infty (lo_1 + lo_2 - \nu_{rf})H(lo_1 + lo_2 - \nu_{rf})\mathrm{d}\nu_{\mathrm{rf}}}{\int_0^\infty H(lo_1 + lo_2 - \nu_{rf})\mathrm{d}\nu_{\mathrm{rf}}}$$

and $H(lo_1 + lo_2 - \nu_{rf})$ is the cross power spectrum of the interferometer ,

Equation 4.15 can be written in terms of the equivalent centroid RF frequency of operation, $\overline{\nu_{rf}}$ as:

$$C(\tau) = \gamma(|\tau_D - \tau|)|G|e^{j(2\pi\overline{\nu_{rf}}(\tau-\tau_D)-2\pi(lo_1+lo2)\tau_D+\phi_{inst})} \tag{4.16}$$

where $\overline{\nu_{rf}} = lo_1 + lo_2 - \overline{\nu_{if}}$

From Equation 4.15 we see that in an SSB system, a discrete change of τ_D produces a phase change equal to $2\pi\overline{\nu_{if}}\tau_D$. Since the phase change depends upon the true value of the centroid $\overline{\nu_{if}}$, we were concerned at the time of the design of the recirculator system about the possibility of unequal bandshapes leading to variations in the centroids. The variations between the frequency responses of different antennas in an array limit the accuracy and the sensitivity of the instrument. The variations in the frequency responses introduce errors in the estimation of the complex gain factors of the antennas. The next section describes the measurements carried out to determine the cross power spectrum of the 512 channels employed for synthesis.

4.2.5.2 Measurement of the cross power spectrum

The cross power spectrum is the Fourier transform of the cross correlation function[13]. We measured the cross power spectrum of all the 512 channels. Figure 4.18 shows the setup used to measure the cross power spectrum. The

---

[13] The cross correlation of two waveforms V_1 and V_2 is defined as $\int_{-\infty}^{\infty} V_1(t)V_2^*(t-\tau)\mathrm{d}t$

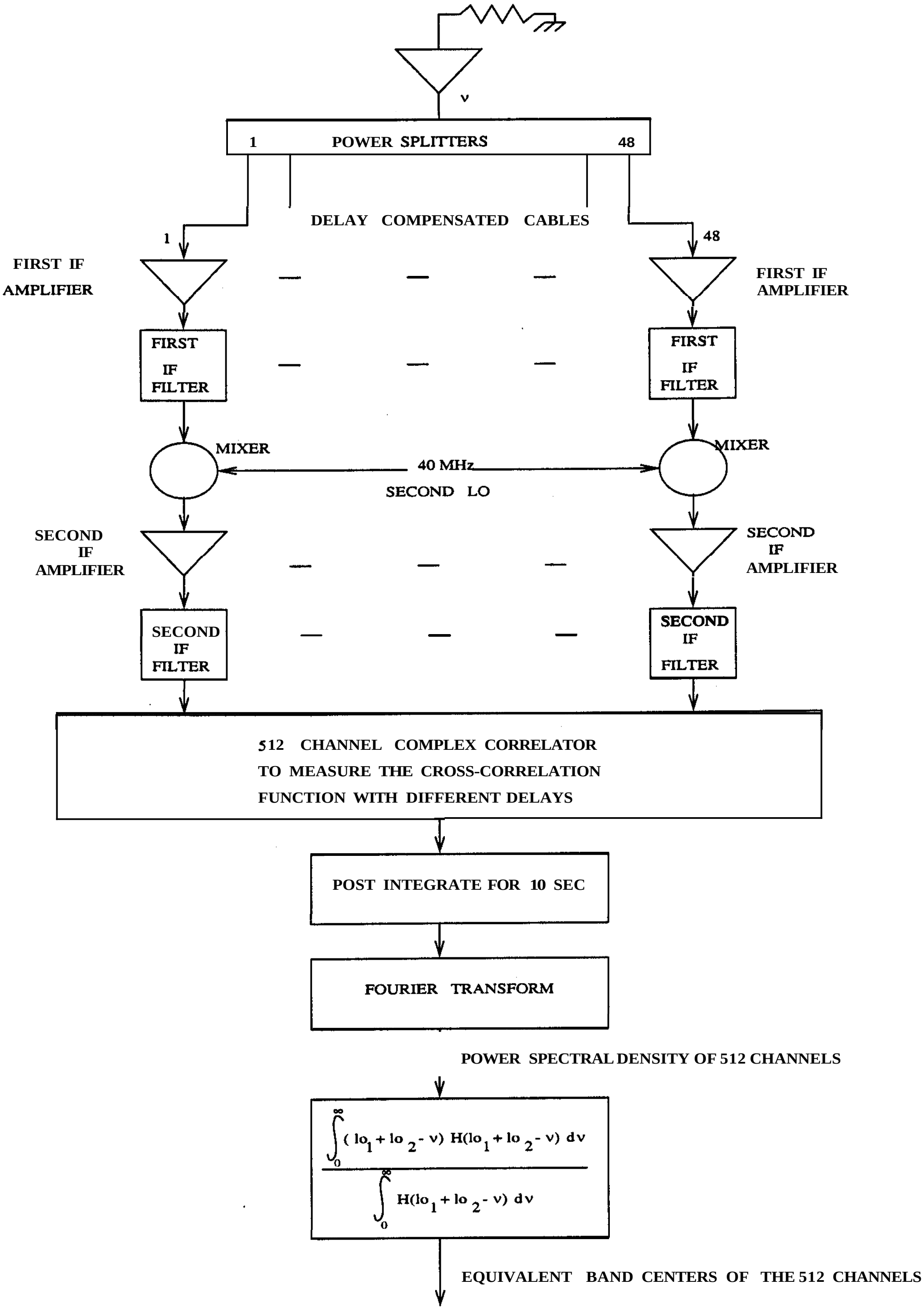

Figure 4.18: The setup used to measure the cross correlation spectra. The different stages of calculating the band-centroids are also summarized here.

cross correlation function with different delays was measured by feeding delay-equalized noise at the input of the second stage mixer unit. The response of the receivers before this stage is much broader and therefore does not affect the centroid. Delays of up to ±3.67 μs in steps of 94.1 ns were used[14]. From the cross power spectrum, an estimate of the band-centroids are obtained by determining their center of gravity. The band-centroids in turn give an estimate of the phase-shift per delay-step used in the IF path. Figure 4.19 shows the different cross power spectra obtained from the cross correlations of the first north-south channel with the 32 east-west channels. The cross power spectrum of the different channels look quite different. For e.g., the first spectrum is somewhat rectangular and has a ripple, whereas the last spectrum looks Gaussian in shape and is smooth. The distribution of all the 512 band-centroids obtained are shown in Figure 4.20. The measurement of the band-centroids was repeated four times at intervals of about 10 days. No noticeable change in the band-centroids was seen.

Most centroids have a value very close to 10.1 MHz while some are in the range 10 MHz to 10.2 MHz. Before this exercise to determine the centroids was done, we had always assumed that all the IF bands were identical and were centered at 10 MHz.

The band-centroids were also estimated from the difference in the instrumental phase in two delay zones on the calibrator MRC 1932-46 on north-south baselines less than —300 m. On these baselines, MRC 1932-46 has a good signal-to-noise ratio in two delay zones. We compare the instrumental phase obtained from independently calibrating the two zones using the same calibrator. Except for the different digital delays, all the parameters are the

---

[14] ±40 delays at **10.625 MHz**

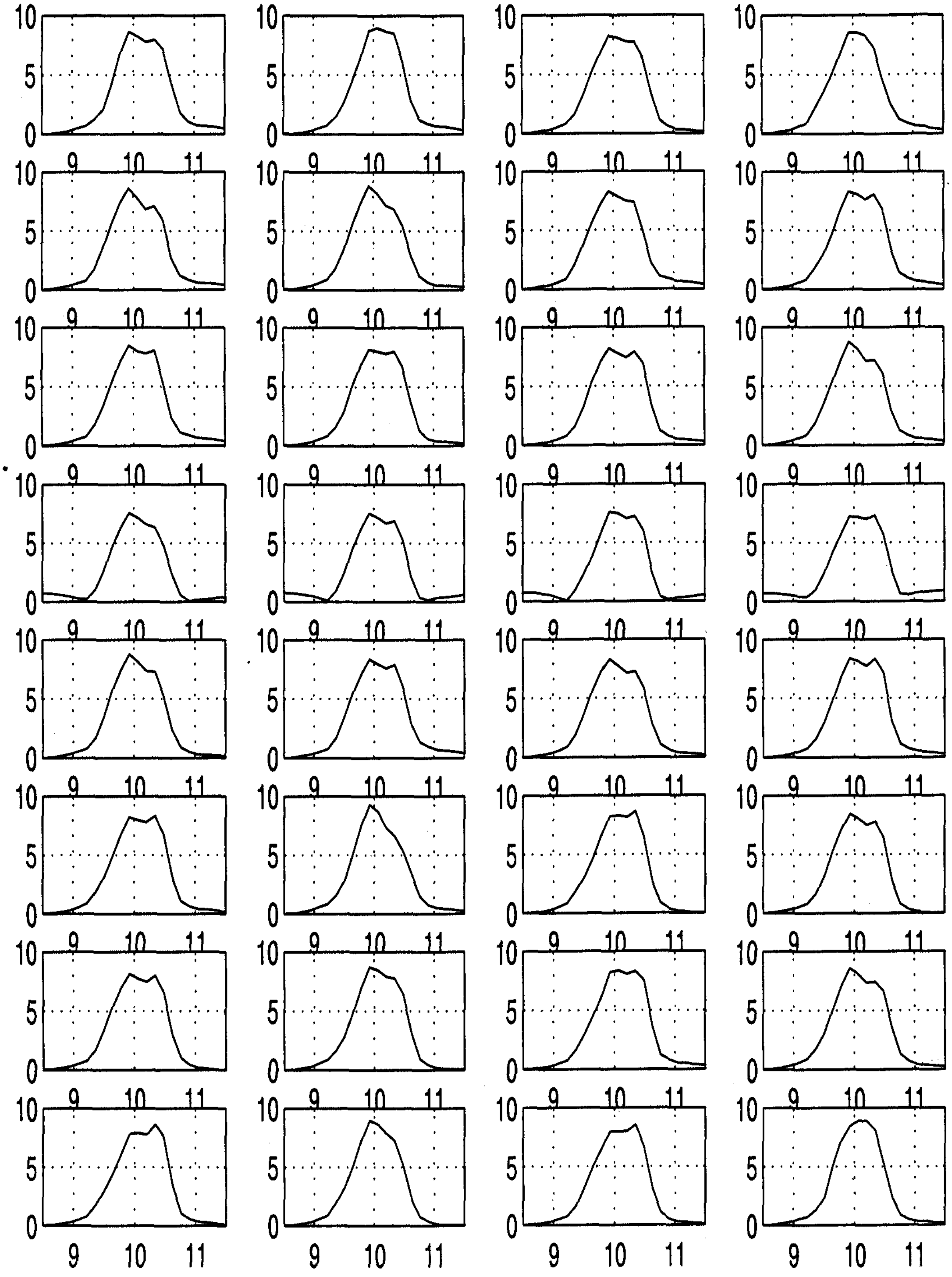

Figure 4.19: The different cross-power spectra obtained from the measurements of cross-correlation of the first north-south channel with all the sixteen east-west channels. The x-axis is the frequency in MHz and the y-axis is the gain.

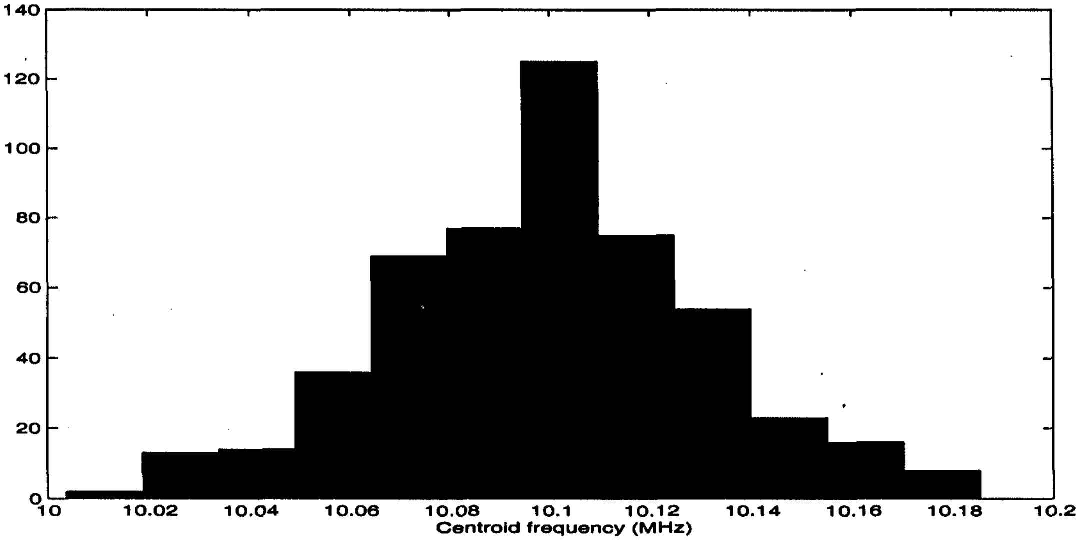

Figure 4.20: Histogram showing the distribution of the centroids estimated by feeding noise in the laboratory.

same in the calibration of the two zones. The difference in phase is only due to the $2\pi\overline{\nu_{if}}\Delta\tau$ term where $A\tau$ is the difference in the delay settings for the two zones. **A** histogram of the difference between the phase per delay of the laboratory measurement and that derived from the source is shown in Figure 4.21. The difference between the phase measurement in the laboratory and that measured on the the source has an RMS of about 5". This is expected as the day-to-day phase variations on the instrumental phase on MRC 1932-46 have an RMS of $\sim 10°$.

Let us discuss the implications of the shift in the centroid by 0.1 MHz and the spread in the centroids.

For baselines up to 172 m, the observations were carried out with delays compensated for the local zenith. The error in phase due to the wrong assumption of an equivalent band-center is given by:

$$\Delta\Phi = 2\pi\delta\nu(\tau_g - \tau_{cal}) \tag{4.17}$$

where $\delta\nu$ is the error in the assumed band-center. τ_g is the geometrical

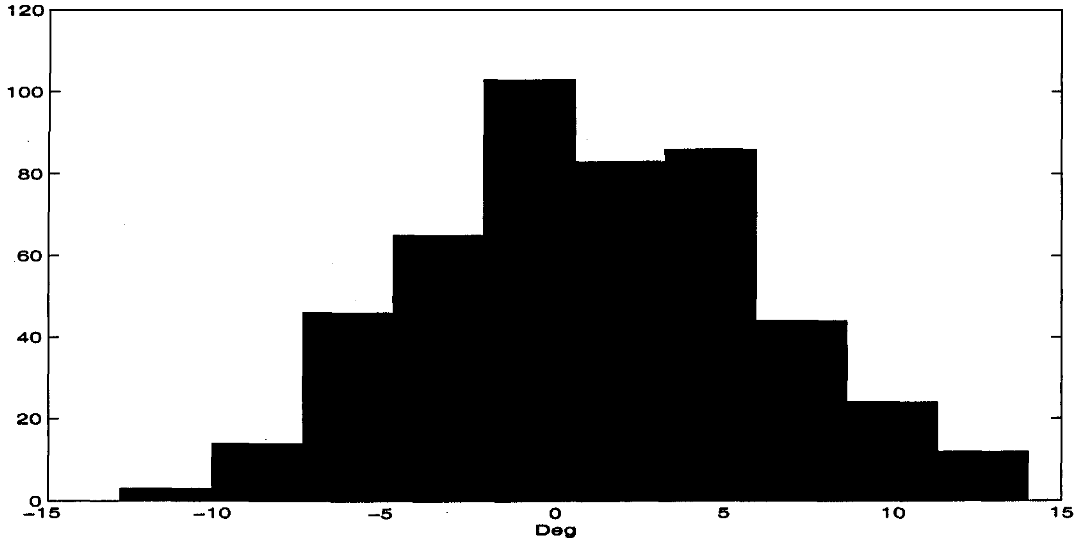

Figure 4.21: Histogram of difference in phase per delay as derived from the laboratory experiment and that from MRC 1932-46.

delay, $\tau_g = \frac{y\lambda\sin(za_\circ)}{c}$. τ_{cal} is the geometrical delay for the calibrator position. y is the north-south baseline (in wavelengths) and $za_\circ$ is the zenith angle along the meridian.

Figure 4.22 shows the error in phase as a function of baseline and declination due to an error of 0.1 MHz in the equivalent center frequency for $\tau_{cal} = 0$, i.e., for a calibrator at $\delta = -20.14°$ and assuming coplanar baselines. So if one had assumed a band centroid of 10 MHz, one would have had errors up to about 15° on some baselines for large zenith angles.

The RMS of the band centroid variation is 0.031 MHz corresponding to an RMS in phase of 5" for a delay of 376 ns (1Delay). The day-to-day and source-to-source phase variations is about $\theta_1 = 10°$. The RMS phase variation per delay due to variations in the band-centroid is about $\theta_2 = 5''$. The net phase error therefore builds to $\sqrt{\theta_1^2 + \theta_2^2}$=11.18. Thus, the spread in the centroid causes the phase errors to increase by only about 10%. The final image is made by combining 32 x 880 visibilities. The dynamic range limitation due to

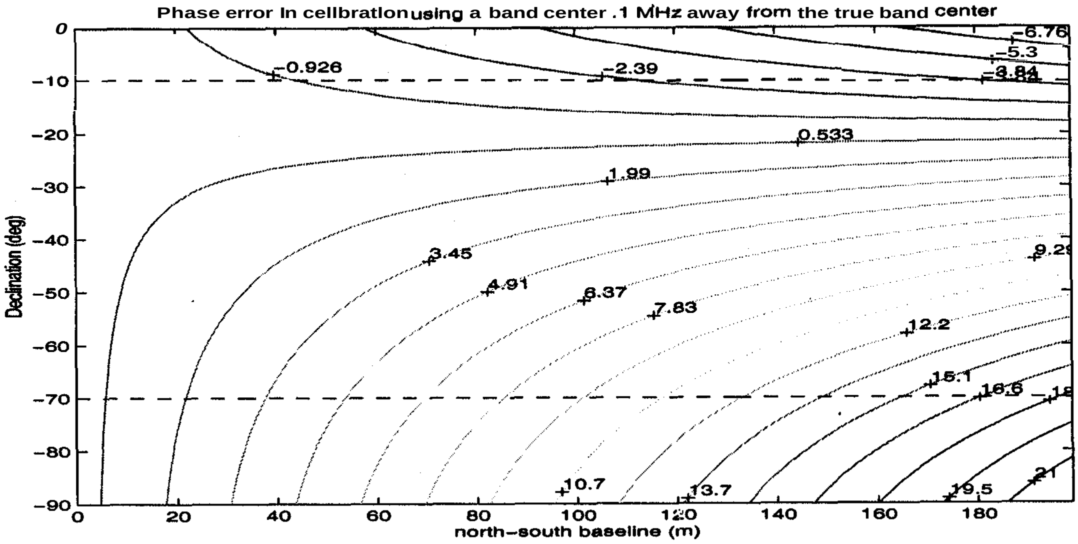

Figure **4.22:** Phase errors (in degrees) in calibration using a band-centroid 0.1 MHz away from the true band-centroid.

a phase error of 11° ($\frac{1}{1.52}$ radians) will be of the order of $\frac{1}{1.52} \times \frac{1}{\sqrt{32\times880}} \approx \frac{1}{850}$. This is quite acceptable. In fact we will be limited in dynamic range mainly due to errors in estimation of the point spread function used to deconvolve the images.

The effect of the change in centroid and the spread in centroid frequency directly causes only a small increment in the phase errors in the final images. However, these affect the images indirectly, such as for estimating the errors using instrumental phase, for e.g., in determining timing and positional errors. Furthermore, in the future, we plan to improve the calibration using multiple source calibration and redundant baseline calibration which are expected to reduce the errors in phase to much less than 5° and therefore would require accurate knowledge of the band-centroids. Hence, we incorporated the different band-centroid measurements in the calibration[15] program and also in the imaging programs.

---

[15] Unequal bandshapes also limit the use of closure phase in calibration and in deriving antenna based gains from baseline based gains.

4.3 Transforming the visibilities to brightness distribution

The MRT has grating responses due to discrete sampling of the visibilities. These influence the way the transformation of the visibilities to brightness is implemented. We therefore look at the effect of grating responses before going on to the implementation of the transformation of the visibilities to brightness.

4.3.1 Grating Response

At the MRT there are grating responses due to

- the discrete sampling of the visibilities, i.e., at 64 m intervals in the east-west arm and ~1 m interval in the north-south arm.
- the basic construction of each group, i.e., each east-west group comprises of 32 helices spaced at 2 m along the east-west and each north-south group is made of 4 helices spaced at 2 m along the east west.

4.3.1.1 Grating responses due to discrete sampling of the visibilities

The FWHM of the primary beam response of an east-west group is 2" (HA= ±1°). This limits us to imaging only this region of the sky at any given time. The sampling of the visibilities in the east-west direction is at intervals of 64 m. This is also the size of an east-west group. When synthesizing on the meridian, this results in grating responses at intervals $\Delta\xi = \frac{\lambda}{64}$. These grating responses fall at the null points of the primary beam response of the east-west group (Figure **4.23).** When the beam is synthesized away from the meridian, the grating responses fall within the primary beam of the east-west group. This is shown in Figure 4.24. Here, the beam is synthesized at an hour angle **1.2**" from the meridian. Sources at hour angle 1.2" get aliased with sources at hour angle –0.575" in the main beam. Furthermore, the contribution from the grating response in the sidelobes also gets aliased. The synthesized beam (including the aliasing) varies with the hour-angle at which it is synthesized. This makes the deconvolution process rather complex. Therefore, at this stage we choose to image on the meridian only, i.e., at $\xi = 0$ (the scanning in right ascension is provided by the motion of the earth).

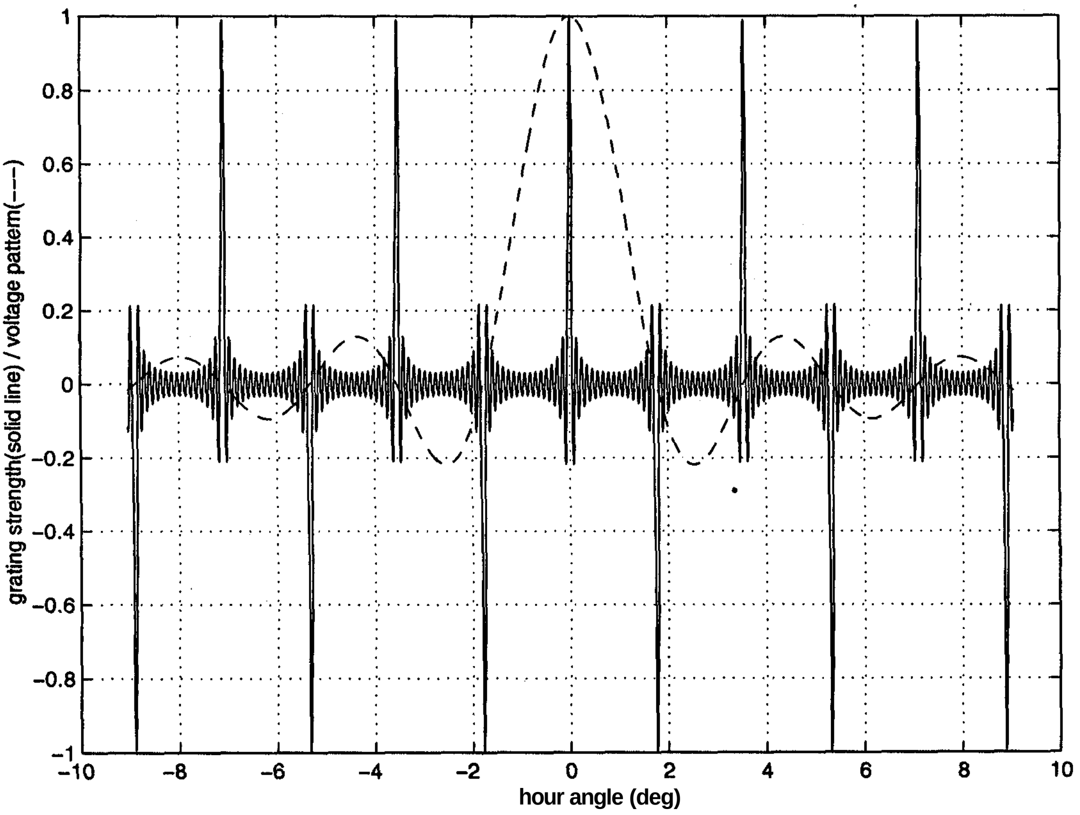

Figure **4.23:** The grating response due to the sampling of the visibilities in the east-west direction in steps of 64 m when the beam is synthesized on the meridian. The voltage pattern of an east-west group is shown by the dashed line. The grating beams lie on the nulls of the east-west voltage pattern.

As already mentioned, the visibilities along the north-south directions are sampled at ~1 m intervals. Due to this sampling we get a grating response at intervals $\Delta\eta = \frac{\lambda}{d_{ns}}$ and in general, the η corresponding to the n^{th} grating

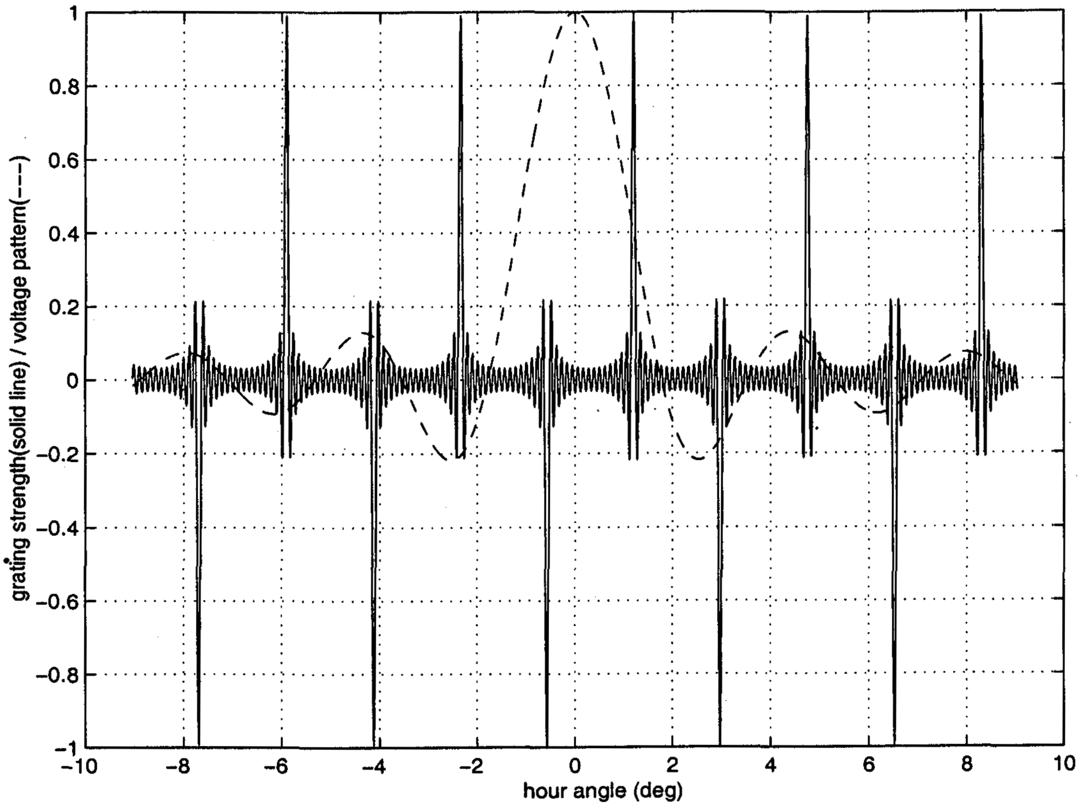

Figure **4.24:** The grating response due to the sampling of the visibilities in the east-west direction in steps of 64 m when the beam is synthesized away from the meridian. The voltage pattern of an east-west group is shown in dashed line. Here, the beam is synthesized at an hour angle 1°.2 from the meridian. Sources at hour angle 1°.2 get aliased with sources at hour angle $-0^\circ.575$ in the main beam. Furthermore, the contribution from the grating response in the sidelobes also gets aliased.

response may be expressed as

$$\eta = n \times \frac{\lambda}{d_{ns}} + \eta_{alias} \tag{4.18}$$

d_{ns}= **1** m is the sampling in the north-south direction,

n is the n^{th} grating response and

η_{alias} is the aliased direction cosine.

This results in the difference between the zenith angle along the meridian (za_o) being imaged and the aliased zenith angle along the meridian to be about 168°. Thus regions $-90^\circ < za_\circ <$ –78.2" are aliased with regions $+78.2^\circ < za_\circ < +90^\circ$. These regions are well beyond the FWHM of the helix response and therefore are not being considered for imaging. However, it is important to note that the sidelobe responses of very strong sources in these regions may affect maps of the regions of interest.

4.3.1.2 Grating response due to the basic composition of the groups

There are grating responses along the east-west direction due to the helices being spaced 2 m (d„) apart in the east-west and north-south groups. These grating responses are at intervals of $\Delta\xi = \frac{\lambda}{d_{ew}}$.

These are in addition to the ones due to the sampling in the east-west being equal to the group size. The two-dimensional response of an east-west group is plotted in Figure 4.25a and a cut along the hour angle at declination zero is plotted in Figure 4.25b. Similar plots of the grating response for a north-south group are plotted in Figure 4.26a and Figure 4.26b. The grating response peaks at an hour angle $H_g = 82^\circ$. From the two-dimensional plot of the response, we note that the grating response peaks in declination at $\delta =$ 0" and falls off at other declinations. Although the grating responses are in the directions where the theoretical beam response of the helix is expected to have an attenuation of about 30 dB, we still see the Sun coming through these grating beams when it is in the declination range $-10^\circ < \delta_{sun} < 10^\circ$. On longer baselines the signal from the grating response gets bandwidth decorrelated. and does not cause a serious problem at longer baselines. Strong sources in this declination range will also contribute to the visibility measurements on short baselines. Since we do not have many strong sources in this declination range, this may not be a serious problem. However, sources like the Sun and the Galactic plane

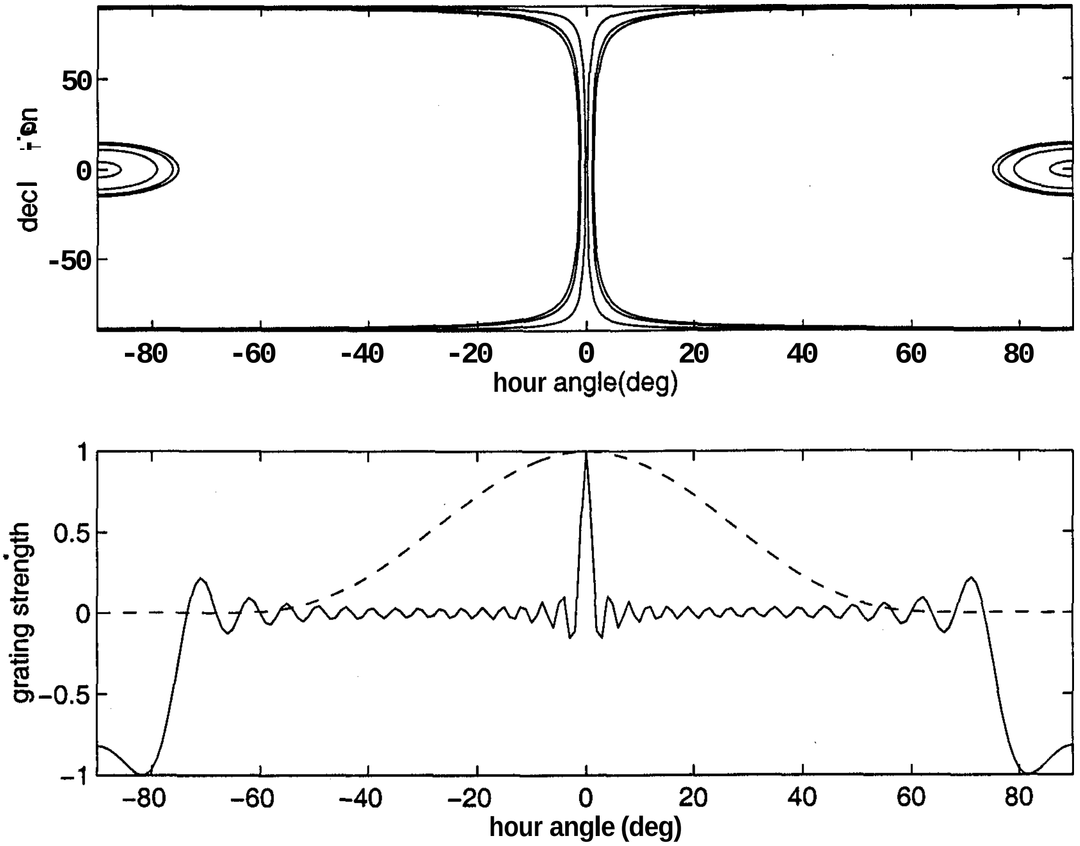

Figure 4.25: The grating response of an east-west group at an operating frequency of 151.5 MHz. (a) The upper plot shows the two-dimensional grating response (the contours levels are [–0.9, –0.5,–0.3, +0.3, +0.5, +0.9]) (b) The lower plot shows a cut along hour-angle at declination zero. The dashed line shows the theoretical primary beam response of a single helix.

in the declination region $-10° < \delta < 10°$ will pose a problem and must be accounted for. In the RA range (1950) from 6h28m to 7h10m and from 18h28m to 19h10m, the galactic plane ($b = 0$) is in this declination range. This would therefore cause the images to be corrupted[16] at RAs which are about 5.47 hours ($H_g = 82°$) away.

A source in the grating response does not appear at its true declination when imaging on the meridian. A source in the grating at an hour angle H_g

---

[16] due to visibilities measured on short baselines being corrupted.

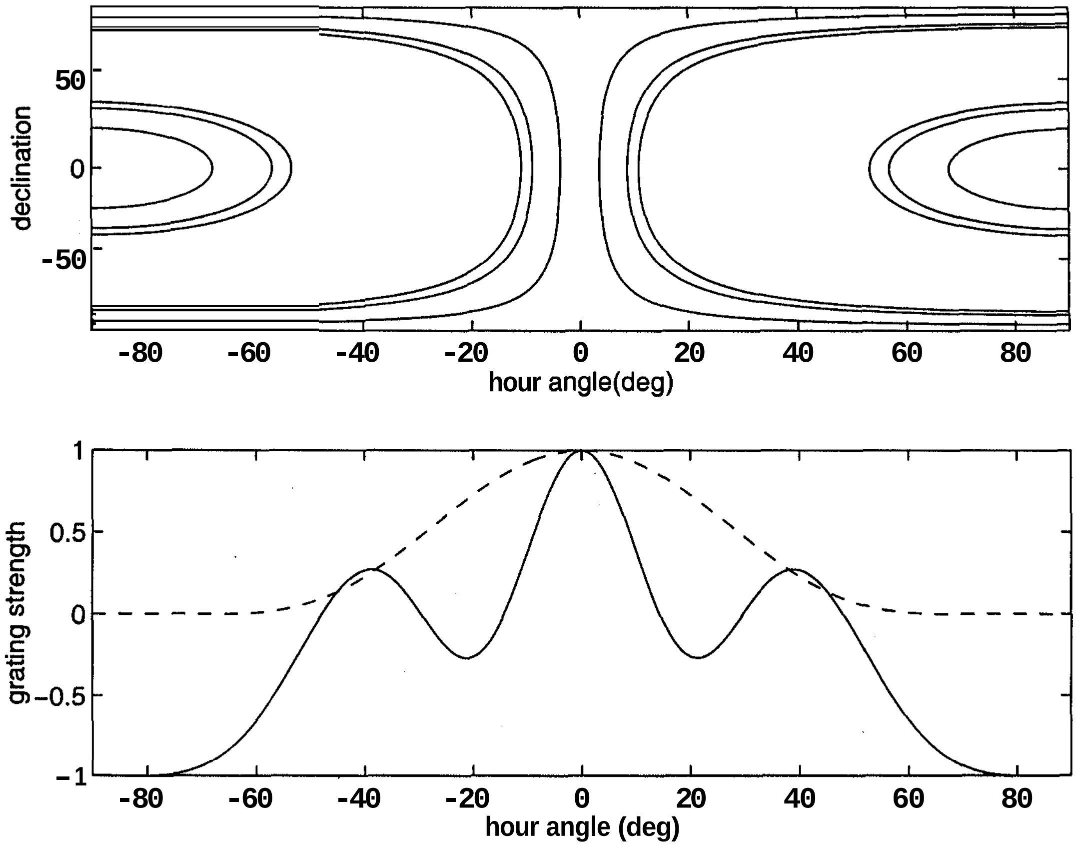

Figure 4.26: The east-west grating response of a north-south group at an operating frequency of 151.5 MHz (a) The upper plot shows the two-dimensional grating response (the contours levels are [–0.9, –0.5,–0.3, +0.3, +0.5, +0.9]) (b) The lower plot shows a cut along hour-angle at declination zero. The dashed line shows the theoretical primary beam response of a single helix.

and declination δ_g has a direction cosine η_g given by (Equation 1.3):

$$\eta_g = \cos\delta_g \cos H_g \sin\phi - \sin 6 \cos\phi \qquad (4.19)$$

where ϕ is the latitude of the telescope. While imaging at meridian transit, i.e., H = 0, the direction cosine η is given by

$$\eta = \sin(\phi - \delta) \qquad (4.20)$$

Therefore, the declination to which a source in the grating gets imaged on the meridian is obtained by equating η_g to η and is given by:

$$\delta = \phi - \sin^{-1}(\eta_g) \qquad (4.21)$$

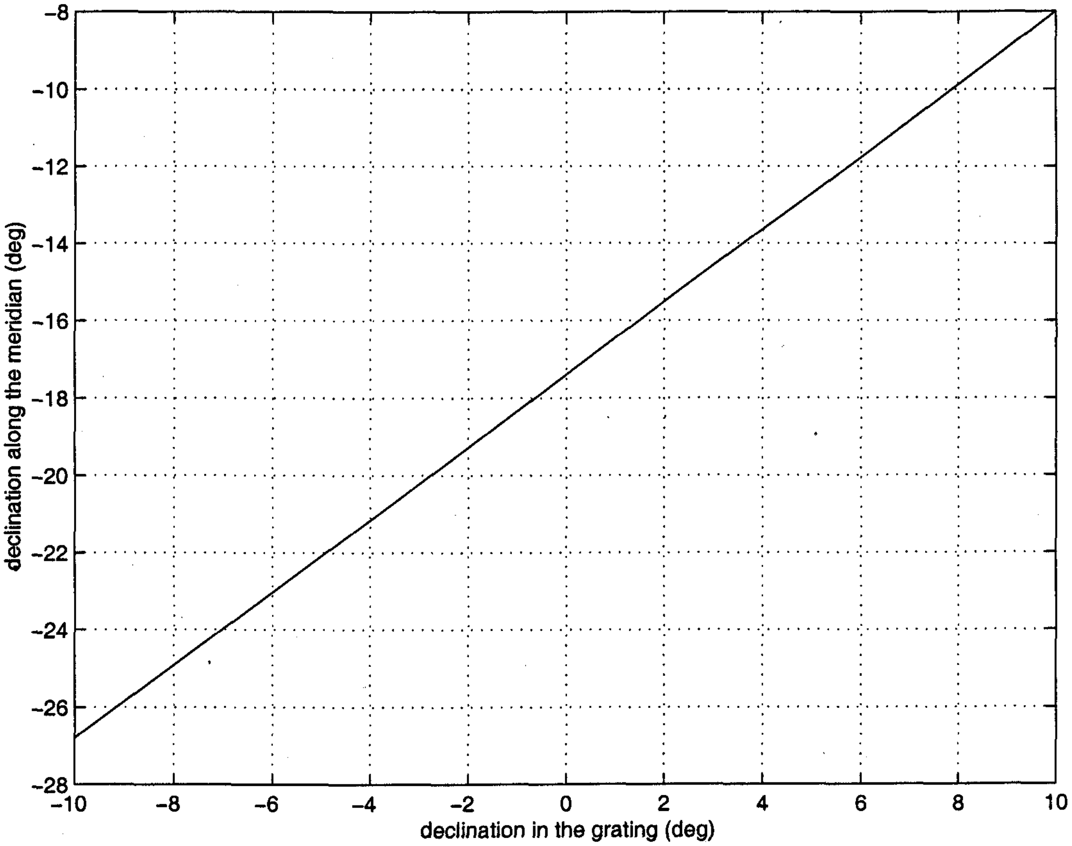

Figure 4.27: The plot shows the translation of declination of a source in the grating to the declination on the meridian for an hour angle of 82°.

Figure 4.27 shows this translation of declination of a source in the grating to the declination on the meridian for an hour angle of 82°.

The RAs and declinations which could be affected by the galactic plane are summarized in Table 4.2. We note that the range of declination affected will depend on the number of east-west groups used for imaging.

RA (1950) when Galactic plane in $-10^\circ < \delta < 10''$	RAs (1950) where this would corrupt the images.	Declination range (1950) corrupted.
06h28m to 07h10m	01h00m to 01h42m : 11h56m to 12h38m	$-27^\circ \leq 6 \leq -8''$
18h28m to 19h10m	23h56m to 00h38m : 13h00m to 13h42m	$-27^\circ \leq 6 \leq -8''$

Table 4.2: Table giving right ascensions and declinations which could be affected by the galactic plane in the grating response.

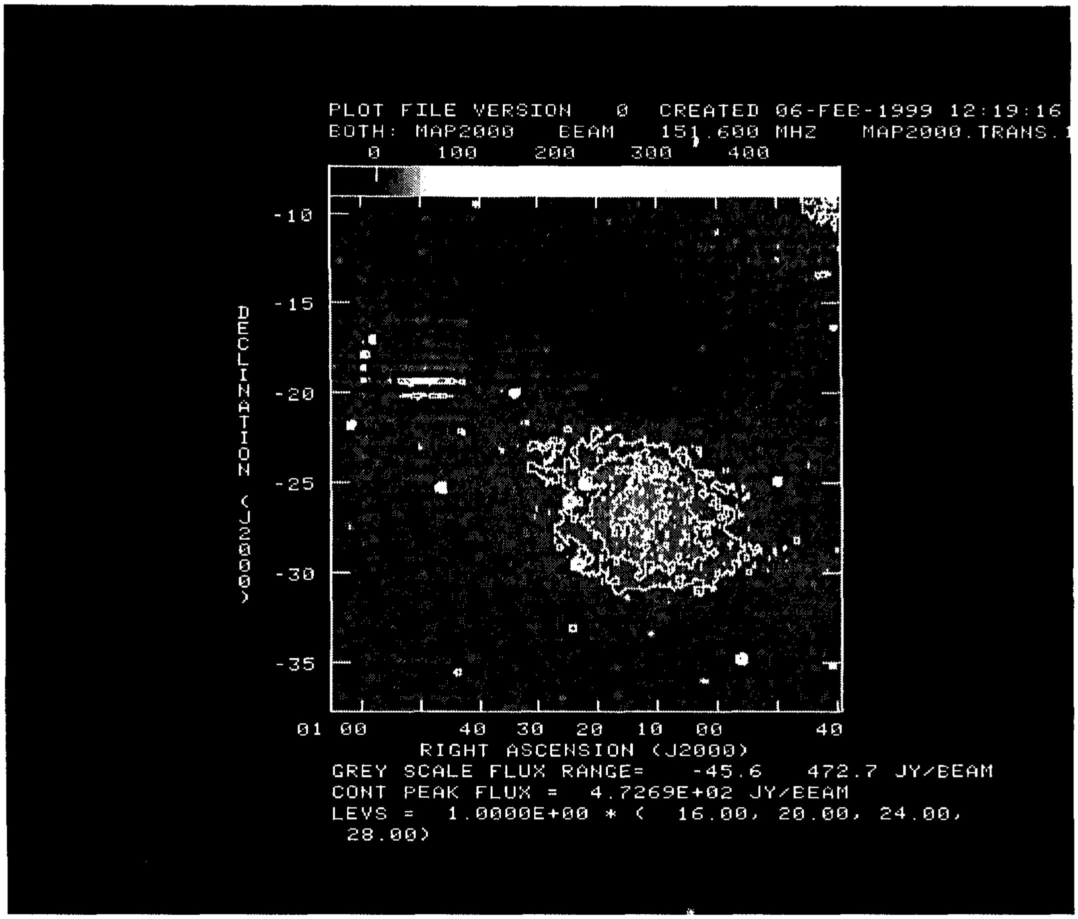

Figure 4.28: The large scale structure seen in the low resolution image of the MRT.

There is a large structure seen [18] in the low resolution images made with visibility measurements of the first two blocks and the central eight groups in the east-west arm. This structure spans RA from 23h55m to 00h30m in the declination range $-32° \leq \delta \leq -23°$. This is shown in Figure 4.28. We now suspect that this structure is due to the galactic plane in the grating response. We have done a rough simulation of the effect of the grating response using the 408 MHz all sky image. The structure in the low resolution image appears displaced in declination from the position seen in the simulation. This can arise because of wrong phasing of the short baselines. There is a huge negative structure to the north of this source which indicates some error in phasing the short baselines. We also expect to see a similar structure spanning RA from 13h00m to 13h42m, when the same part of the galactic plane is in the other grating response. This region however has not been imaged yet. Our simulation does not show any contribution from the grating from the galactic plane in RA range 06h28m to 07h10m. Since this is close to the anti-center position we do not expect much contribution from that direction.

4.3.2 Imaging on the meridian

At the MRT, we are imaging a very large field of view, $\sim$ 60°, with a non-coplanar array. The visibilities measured on the x, y, x plane are related to the dirty image, $B''(\xi,\eta)$ by (Equation 1.17)

$$B''(\xi,\eta) = \frac{A_N(\xi,\eta)B(\xi,\eta)}{\sqrt{1-\xi^2-\eta^2}} \star\star\, b_o(\xi,\eta) =$$
$$\int\int\int W(x,y,z)V(x,y,z)e^{j2\pi\left(x\xi+y\eta+z\left(\sqrt{1-\xi^2-\eta^2}\right)\right)}\mathrm{d}x\;\mathrm{d}y\;\mathrm{d}z$$

Because of the grating response problem, imaging is presently done only at meridian transit, i.e., at $\xi = 0$. So at each instant, i.e., at each RA, we image the complete range of η. Therefore, the dirty image at each instant as a function of η, i.e. $B_t''(\eta)$, may be written as

$$B_t''(\eta) = \int\int\int W(x,y,z)V(x,y,z)e^{j2\pi\left(y\eta+z\left(\sqrt{1-\eta^2}\right)\right)}\mathrm{d}x\;\mathrm{d}y\;\mathrm{d}z \qquad (4.22)$$

At the MRT, the visibility coverage at each instant can be thought of as a pleated sheet, extended in both x and y, with discrete steps in z (height) as we move from one east-west group to another group at a different height.

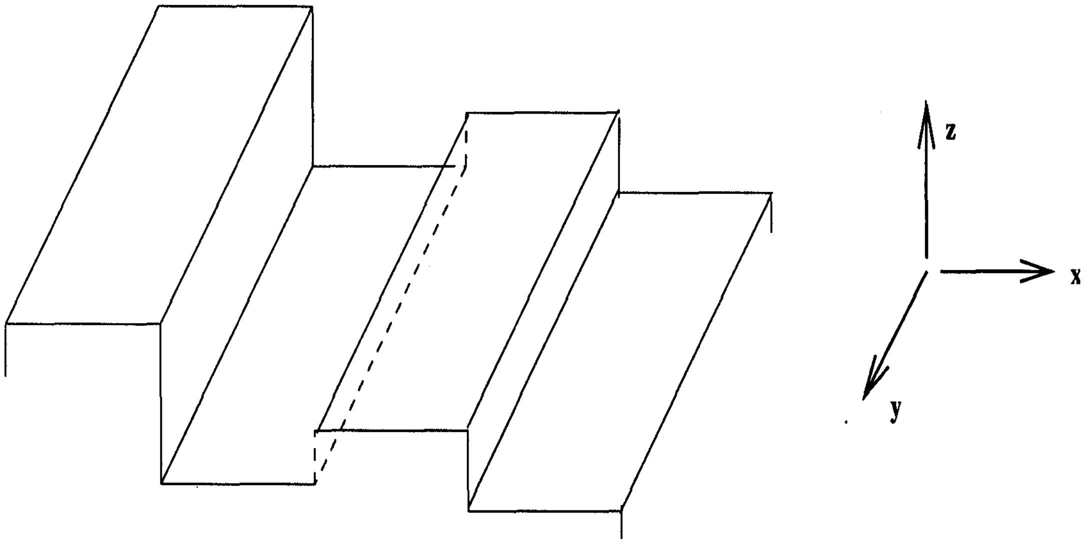

Figure 4.29: A representation of the visibility coverage [2] at the MRT.

Figure 4.29 shows the representation of the visibility coverage at each instant at the MRT.

We have two methods of transforming the visibilities to brightness, i.e., computing the integrals in Equation 4.22. The first method uses a combination of the FFT, for the integral w.r.t y in Equation 4.22, and direct phasing along the z axis. In this, we assume that the y-axis is uniformly sampled. The second method uses only direct phasing – a brute-force approach. There are no assumptions made about uniform sampling but is somewhat expensive in terms of computer time[17]. The two methods are discussed in the following subsections.

4.3.2.1 Implementation using the FFT

Here we transform the visibilities using a Fast Fourier Transform (FFT) along the y-axis assuming it is regularly sampled, apply direct phasing along the x-axis and finally sum along the x-axis to obtain the image on the meridian.

---

[17] **An FFT requires N $\log_2$ N computations as opposed to N^2 for direct phasing.**

The phasing along the z-axis corrects every term along the zenith angle on the meridian for the group heights. This is equivalent to phasing the groups to a common (and artificial) 2D plane.

The north-south array slopes (Figure 2.11) downwards at about $\frac{1}{2}^{\circ}$ to the horizontal from 10 m till about 655 m, and then slopes upwards at about 1° to the horizontal. The north section is flat. These three parts are to be treated separately while transforming. The slope has to be taken into account by assuming an instrumental zenith appropriate to the slope of the track. While combining contributions from different parts, we need to introduce the necessary corrections to get an instrumental zenith equal to the latitude of the MRT.

4.3.2.2 Implementation using direct phasing only.

In this method, the calibrated visibilities are re-phased for each point in the sky at transit ($\xi = 0$) and combined to get the dirty image at that point.

This may be represented as follows:

$$B_t''(\eta) = \sum_x \sum_y \sum_z V(x, y, z) \times e^{j2\pi\left(y.\eta + z.\sqrt{1-\eta^2}\right)} \tag{4.23}$$

where $B_t''(\eta)$ is the dirty image at time t.

The images presented in this thesis are transformed using the second method. The measured height and distance along the track were used without assuming any particular value for the slope of the track and without assuming a uniform sampling of the visibilities in any direction. Therefore there is no need to treat different parts of the track with different slopes separately.

The visibility data observed has hermitian symmetry since the image is real. Instead of generating the hermitian symmetric visibility data we can get the same result by taking only the real part of above data. The imaginary part of the data is also generated and is used to check the calibration by making sure the imaginary part is zero at the transit time of the calibrator.

4.4 Combining different sets of observations

4.4.1 The problem of different precession

Since we observe different baselines on different days, we have to combine data of different observations spread over 2 years. The precession on different sets being combined could be very different. We therefore precess the images of each observation to a common epoch before combining different sets of data. There is the danger of precessing dirty images which causes the sidelobes to be precessed differently than the source[18]. Combining images with different baseline data may therefore cause smearing of the image. Figure 4.30 [3] shows the precession in right ascension per year for different RAs and declinations. We note that at a right-ascension of 19 hr, the contributions of a source at $6 = -10^\circ$ and $6 = -70^\circ$ will be differently precessed by about 4 seconds in one year. This information can be included in the determination of the point spread function used to deconvolve the images. For now, to reduce the smearing we choose an epoch at the midpoint of the observations and then precess the final images to the required epoch[19].

4.4.2 The problem of different bandwidth decorrelations

The other aspect of combining the data is due to different bandwidth decorrelations at different positions along the north-south direction. The east arm and the west arm have different cable lengths. This results in different decorrela-

---

[18] Another source of error which perhaps is only of academic interest because it is very small is that the different primary beam corrections will be different over different epochs.

[19] Ideally the final precession should be done only after deconvolving the images.

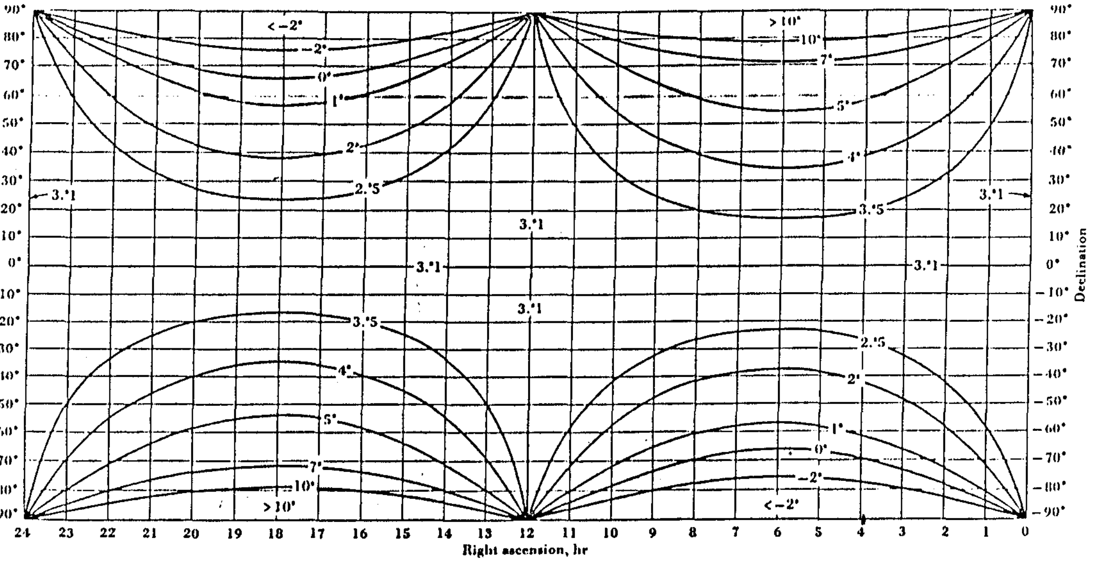

Figure 4.30: Right-ascension precession in seconds of time per year [3]

tion for these arms. Figure 4.31 to Figure 4.33 shows the average decorrelation for observations in the different blocks for the different delay settings. The dotted lines show the average decorrelation on the east groups, the dashed lines indicate the average decorrelation for the west groups. For block-1 and block-2 there is only one delay setting. For block-3 there are 2 delay settings, for block-4 there are 3 delay settings and for block-5 onwards there are 4 delay settings. To keep the bandwidth decorrelation to less than 5%, we have made four sets of images by combining data of block-1 and block-2 with data from different delay zone in block-3, block-4 and block-5. The four images are labeled as L1, L2, L3 and L4 where

- L1 is the image made using data from block-1, block-2 and zone-1 data of block-3, block-4 and block-5.
- L2 is the image made using data from block-1, block-2, zone-1 data of block-3 and zone-2 data of block-4 and block-5.
- L3 is the image made using data from block-1,block-2, zone-2 data of

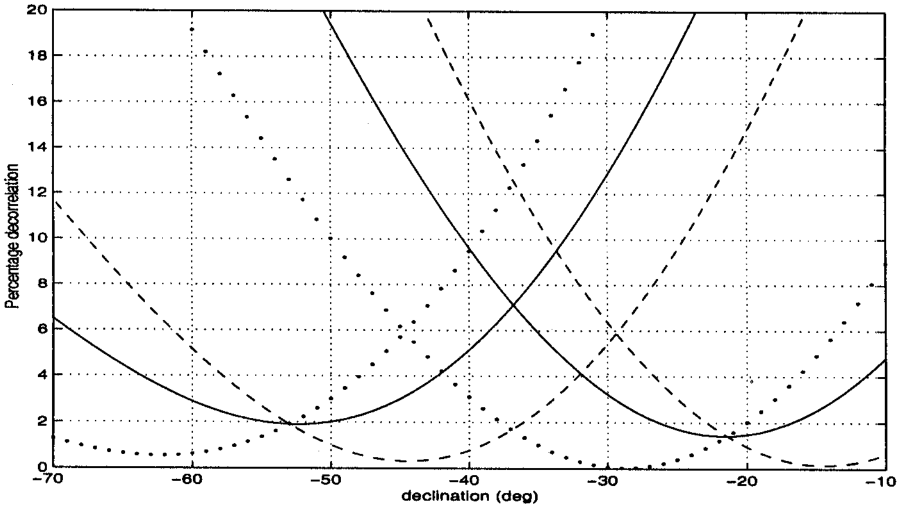

Figure 4.31: Average decorrelation for the two zones in block-3 (172 m-261 m). The dotted line is for the average decorrelation on the east groups, the dashed line is the average decorrelation for the west groups and the solid line is the average decorrelation for all the groups.

block-3 and zone-3 data of block-4 and block-5.

- L4 is the image made using data from block-1,block-2, zone-2 data of block-3, zone-3 data of block-4 and zone-4 data of block-5.

The different combinations used are summarized in Table 4.3. The average decorrelation can be kept to within 5% by choosing the appropriate combination for imaging a given declination region. Figure 4.34 shows the average decorrelation on the images made by combining different delay zones.

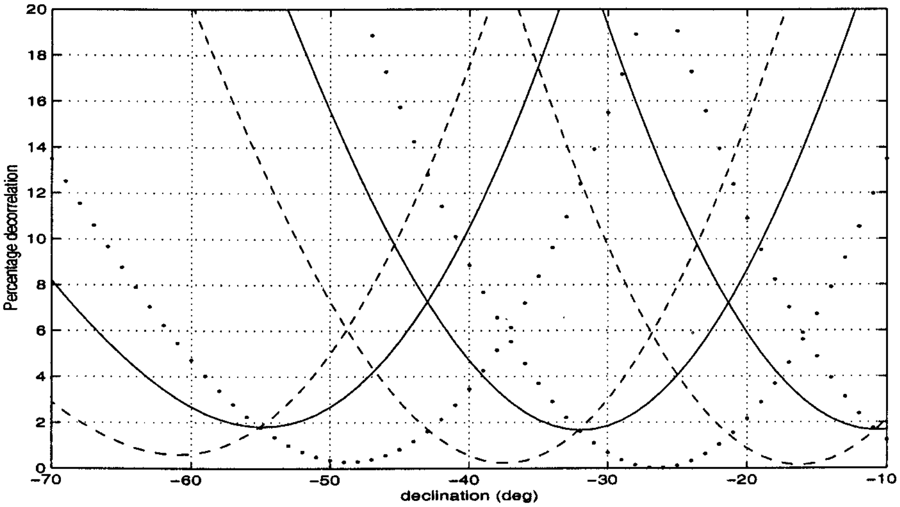

Figure 4.32: Average decorrelation for the three zones in block-4 (262 m-351 m). The dotted line is for the average decorrelation on the east groups, the dashed line is the average decorrelation for the west groups and the solid line is the average decorrelation for all the groups.

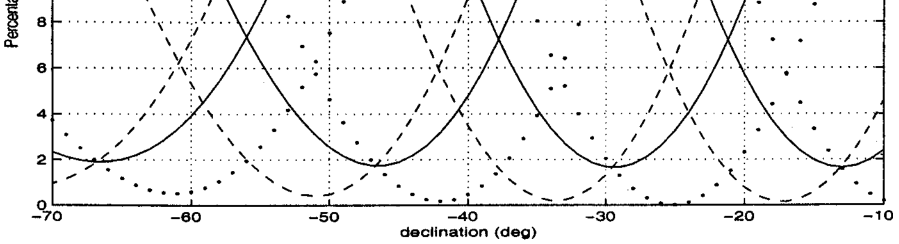

Figure 4.33: Average decorrelation for the four zones in block-5 (352 m-441 m). The dotted line is for the average decorrelation on the east groups, the dashed line is the average decorrelation for the west groups and the solid line is the average decorrelation for all the groups.

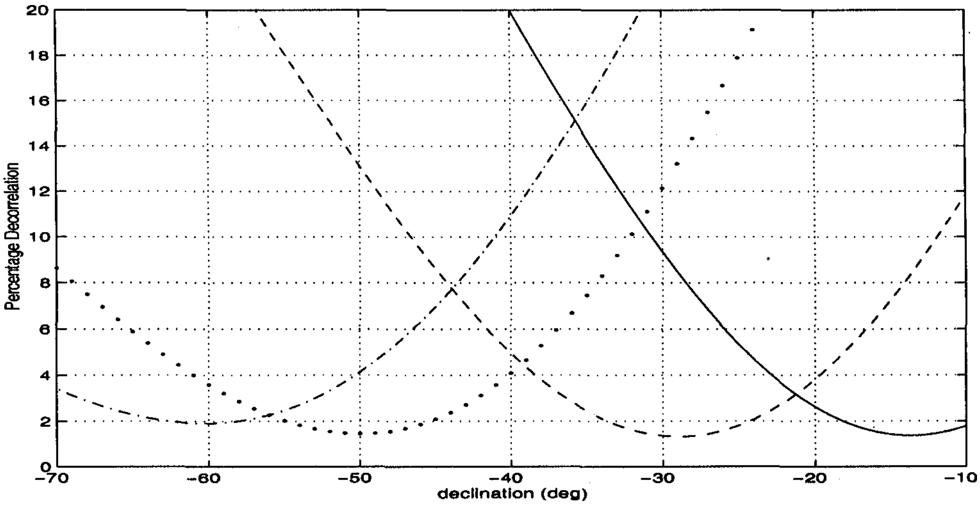

Figure 4.34: Average decorrelation on the images made by combining different zones of data in each block. The solid line is the decorrelation for L1. The dashed line is the decorrelation for L2. The dotted line is the decorrelation for L3. The dot-dashed line is the decorrelation for L4. L1, L2, L3, L4 are summarized in Table 4.3.

	block-3	block-4	block-5	6 range for decorr. $\leq 5\%$
L1	zone1	zone1	zone1	$-25° \leq \delta \leq -10°$
L2	zone1	zone2	zone2	$-41° \leq \delta \leq -18°$
L3	zone 2	zone 3	zone 3	$-62° \leq 6 \leq -38°$
L4	zone 2	zone 3	zone 4	$-70° \leq 6 \leq -48°$

Table 4.3: Table summarizing the combinations of block-1 and block-2 images with different delay zone images of block-3, block-4 and block-5. The last column gives the declination range for which the average decorrelation is less than 5%.